



---

# Analysis and wavefront reconstruction of a high-power laser focus

---

Master thesis

by

**Enrico Ridente**

04.10.2017

**Ludwig-Maximilians-Universität München**

Faculty of Physics

Chair of Medical Physics

Laser Ion Acceleration

---

*Supervisors:* Prof. Dr. Jörg Schreiber, Daniel Haffa



---

# Analyse und Wellenfrontrekonstruktion des Fokus eines Hochleistungslasers

---

Masterarbeit

von

**Enrico Ridente**

04.10.2017

Ludwig-Maximilians-Universität München  
Fakultät für Physik  
Lehrstuhl für Medizinische Physik  
Laser-Ionen-Beschleunigung

---

*Gutachter:* Prof. Dr. Jörg Schreiber  
*Betreuer:* Daniel Haffa

# Contents

<b>Contents</b>	<b>v</b>
<b>Abstract</b>	<b>vii</b>
<b>1 Introduction</b>	<b>1</b>
1.1 Structure of the thesis . . . . .	3
<b>2 Theory of laser focusing</b>	<b>5</b>
2.1 Light propagation . . . . .	5
2.1.1 The Rayleigh-Sommerfeld diffraction theory . . . . .	5
2.1.2 Fourier optics . . . . .	8
2.2 The off-axis achromatic aberration . . . . .	9
2.2.1 The diffraction theory of aberration . . . . .	9
2.2.2 The Zernike polynomials . . . . .	12
2.3 The Gaussian beam . . . . .	13
2.4 Laser-driven ion acceleration . . . . .	15
2.4.1 Plasma physics . . . . .	16
2.4.2 Damage threshold and laser contrast . . . . .	18
2.4.3 Optical probing . . . . .	19
<b>3 The laser focus spatial intensity distribution</b>	<b>21</b>
3.1 High dynamic range focus pictures . . . . .	21
3.2 Camera characterisation . . . . .	23
3.3 Overview and issues . . . . .	31
3.3.1 The pixel-scheme . . . . .	31
3.3.2 Results and further applications . . . . .	31
<b>4 A semi-automatic focus adjustment procedure</b>	<b>33</b>
4.1 The 90° OAP . . . . .	33

4.2	OAP positioning system; the Hexapod . . . . .	35
4.3	Focus adjustment procedure . . . . .	38
4.4	A program for the alignment routine . . . . .	39
4.4.1	Relative positions . . . . .	41
4.4.2	Calibrate . . . . .	42
4.4.3	Tip-Tilt . . . . .	43
4.4.4	Settings . . . . .	44
4.4.5	Drawing/SOC . . . . .	45
4.4.6	Focus analysis . . . . .	45
4.5	Further improvements . . . . .	47
<b>5</b>	<b>Wavefront retrieval from intensity distributions</b>	<b>49</b>
5.1	How to obtain a flat wavefront in focus . . . . .	49
5.2	Wavefront retrieval methods . . . . .	51
5.3	The role of the propagators in the wavefront retrieval algorithm program	53
5.3.1	Main dependencies of the algorithm . . . . .	55
5.4	Final results and further improvements . . . . .	59
<b>6</b>	<b>General conclusions and further developments</b>	<b>63</b>
<b>Appendix</b>		<b>65</b>
	Ideal wavefront calculation (Matlab script) . . . . .	65
	Centroid (Matlab script) . . . . .	66
	Wavefront retrieval algorithm (Matlab script) . . . . .	68
	Manual for the focus adjustment procedure . . . . .	71
<b>List of Figures</b>		<b>83</b>
<b>Bibliography</b>		<b>84</b>
<b>Acknowledgments</b>		<b>88</b>

# Abstract

In this thesis the importance of the laser focus for a laser driven ion-acceleration experiment is presented. The improvement of its quality, in order to reach higher ion energies, has been the main motivation behind this work.

Specifically, two programs have been developed to better characterise the laser focus; a software tool for easy focus alignment, written in LabVIEW; and a Matlab code to retrieve its wavefront. The measurements and the experiments have been conducted in the Laser-ION (LION) acceleration cave in the Laboratory for EXtreme photonics (LEX) in Garching bei München with the ATLAS-300 laser. Additional developments have been executed in the Medical Physics laboratories close to LEX.

The LabVIEW program allows for a quantitative characterisation of the focus shape and is able to easily correct for astigmatism, which is achieved by coupling the axes of the Hexapod. This is the positioning system on which the final focusing off-axis-parabolic (OAP) mirror of the laser-plasma experiment is mounted. The program will be used for the OAP alignment procedure in the new Centre for Advanced Laser Applications (CALA).

To optimise the energy in the focal spot, the beam not only needs to be well aligned but also free from any wavefront distortion, called aberration. This condition is strictly related to the flatness of the wavefront in the focal plane. Ideally, the beam should have a flat wavefront in focus and a Gaussian intensity distribution. Wavefront reconstruction is necessary to characterise the aberration and correct for it. The Matlab code developed retrieves the wavefront starting from intensity distributions in and out of focus. The reconstruction provides also information in planes not directly detected by the beam imaging system. Its precision is only limited by the quality of the optics used. This method has been successfully applied to a high-power laser beam after the last focusing optics.



# 1 Introduction

Charged particles are accelerated in electric fields. The developments, which started in 1889 with electromagnetic propulsion from E. Thomson, have grown into the modern Radio-Frequency (RF) cavities commonly used today. These 'conventional' accelerators struggle for a source capable of generating high-electric fields at higher frequencies, they require longer acceleration lengths to reach higher energies. Laser light is an interesting consideration in this case. High field strengths can easily be achieved today by focusing a short pulse laser to a tight spot, which leads to field strengths of TV/m.

The idea of using electric fields produced by lasers is already two decades old, a detailed history can be found in [1]. Using a laser as the source of energy leads to several unique characteristics of the accelerated particle bunches, as the broad energy spectrum and the high fluence. Furthermore, the relative compactness and low cost compared to conventional accelerators has pushed the experiments towards numerous applications, as:

- Inertial Confinement Fusion (ICF). This benefits from the short bunch duration to provide a fast ignition process [2].
- Imaging. High spatial resolution can be attained, because of the smallness of the emitting proton source [3].
- Ion therapy. The protons, accelerated by the laser, can reach energies of tens of MeV. This could be already enough to irreversibly damage DNA [4] and irradiate superficial but not deep tumours (energy required to go through 30 cm water:  $\sim 200 \text{ MeV}$ ) [5].

The reason for the uniqueness of these proton characteristics is the acceleration process. An optimal laser-driven ion accelerator would convert all incident laser energy into kinetic particle energy. Still a lot of improvements need to be done to optimise this process. A high electric field gradient leads to a strong acceleration, and the maximal

electric field gradient can be achieved, if all spectral and spatial components of the laser pulse interfere constructively in the focus.

ATLAS-300 is a 25 fs, 7.5 J (300 TW) Ti:Sa laser system, based on chirped-pulse-amplification [6]. These parameters make it suitable for laser-driven ion acceleration. One of the main factors which limits its achievements is the loss of two third of the laser energy on the way from the compressor to the target. Here, the absorption due to the optics cannot justify why more than half of the initial energy cannot reach the target. The reasons for this energy loss can be found in the imperfections on the mirrors and focusing optics surfaces and in their misalignments. Both these effects result in a change from the ideal spatial intensity distribution (SID), in other terms, in an aberration. Looking at figure 1.1, a clear correlation between SID and wavefront emerges. Therefore, characterising this information directly on target is crucial if we want in turn to correct for aberration. These corrections would result in a cost-efficient way of having higher energy on target, without having to compensate with even more incident laser energy.

This thesis will be centred on the focus adjustment procedure to correct for misalignments of the focusing optics and on the wavefront reconstruction out of SIDs.

A similar technique, as the one just mentioned, is used to retrieve the wavefront in coherent X-ray diffraction imaging [7], image encryption [8] and in astronomy [9]. Here, the wavefront distortion induced by the atmosphere can be indeed retrieved and pictures taken from a telescope on earth can be adjusted. Furthermore, the aberration due to mirrors along the beam path can be corrected in the calculations, reducing drastically their cost because of the lower precision needed in their making process.

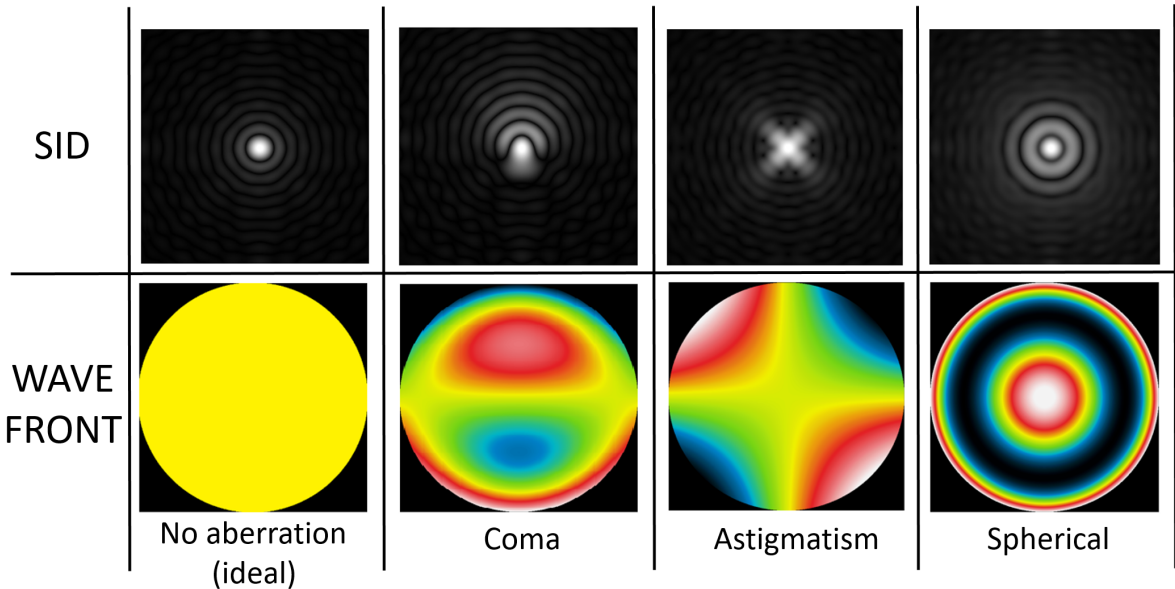


**Figure 1.1:** The picture shows how a flat-top SID with a flat wavefront changes, on the focal plane of a thin lens, as a function of the aberration in the optical system. Only in the ideal case the highest intensity in the central spot can be reached. Picture edited from [10].

## 1.1 Structure of the thesis

The importance of the focus SID will be the main topic which will guide the reader through this work. At the beginning, the theoretical background behind diffraction theory and aberration will be presented (2nd chapter). A HDR (High Dynamic Range) camera will be the topic of the 3rd chapter. This is namely able to get a full characterisation of SID in a single frame. In the 4th chapter the Hexapod, a special positioning system, will be analysed. Because it is the support of the last focusing optics, correcting for misalignments means moving the Hexapod properly. For this purpose, a LabVIEW program has been developed. It is a useful tool to characterise and make the chase for best focus faster and easier. In the 5th chapter an algorithm to retrieve the wavefront from SIDs in and out of focus will be shown. In conclusion, a summary of the results obtained and their possible developments will be presented in the 6th chapter.



## 2 Theory of laser focusing

The advent of high-power laser systems allowed for further investigations of laser-plasma interactions in the relativistic ( $> 10^{18} \text{ W/cm}^2$ ) regime [11]. Conventional accelerators suffer from spark-induced breakdown, whereas in a laser-induced plasma the atoms are already separated and this limit is not in place. This makes thinking about laser-driven accelerators a valuable opportunity. To ensure maximum energy transport from the light source to the designated target, and to provide maximum intensity, a lot of caution has to be paid to the transport of the laser light. It is transmitted and reshaped via transmissive and reflective optics, which can either be flat or have focusing capabilities. In a real world scenario, these optics can be manufactured with a very high but still limited precision. This is a big cause for energy loss, as the light is not following the optimal path.

The ideal case will be examined in the first section and, in particular, the theoretical background behind focusing a spatially broad beam. Deviations from the ideal path, which result in aberration, will be the topic of the second section. In the third section a “special” beam will be studied, the Gaussian beam. Finally, in the forth section the effects of the laser focus on the laser-driven ion acceleration will be considered.

### 2.1 Light propagation

#### 2.1.1 The Rayleigh-Sommerfeld diffraction theory

To study how a beam is altered by the aberration, we first have to understand how it should look like in the image plane. The ideal case can be obtained resorting to the diffraction theory. Generally speaking, all the phenomena resulting in a change of the light propagation, due to a mask with a transmission function different from one, can be described by it. Starting from a known ideal aperture and a known electric field  $\vec{E}$ , this theory allows to calculate  $\vec{E}$  in any plane positioned after the aperture. This theory only takes the wave nature of light into account and, wherefore, the Huygens-Fresnel principle can be applied. It states that a broad beam can be seen as an ensemble of point sources, emitting coherently in  $2\pi$  towards the Poynting vector direction. To

obtain the form of  $\vec{E}$  in any point  $P$  after the aperture, the parameters in figure 2.1 have been used.

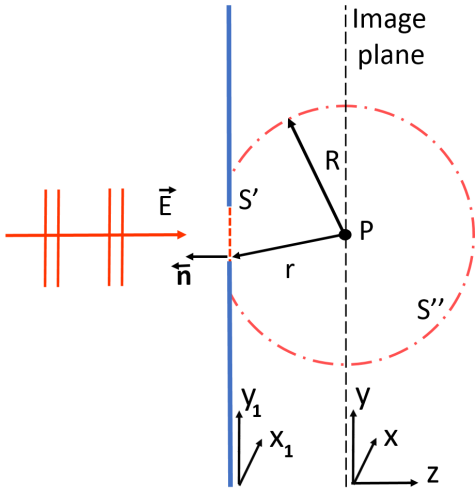


**Figure 2.1:** A screen, with a transmission function equal to 1 in  $S'$  and 0 elsewhere, is set along the path of a monochromatic beam. The section of the beam has to be wider than the surface  $S'$  in order to generate a diffraction pattern. Picture edited from [12].

In the picture above, a beam with an electric field  $\vec{E}$  passes a two dimensional aperture of size  $S'$  and normal  $\vec{n}$ . A sphere of radius  $R$  is centred in  $P$ , a point on the image plane. To include also the aperture plane in our calculations,  $R$  has been chosen bigger than  $r$ , which is the distance from  $P$  to a generic point of the aperture.

Starting from the wave equation:

$$\left(\nabla^2 - \frac{1}{c^2} \frac{\partial^2}{\partial t^2}\right) \vec{E}(\vec{s}, t) = 0 \quad (2.1)$$

and separating the spatial dependency,  $\vec{s}$ , from the temporal one,  $t$ , the Helmholtz equation can be obtained:

$$(\nabla^2 + k^2)U(\vec{s}) = 0 \quad (2.2)$$

where  $k = \frac{2\pi}{\lambda}$ .

The goal is to find a solution for  $U(P)$ .

A useful mathematical tool, which fits our problem, is Green's theorem. A smart choice for the Green function is reported in the equation below:

$$G = \frac{e^{-ik|\vec{r}|}}{|\vec{r}|} - \frac{e^{-ik|\vec{r}'|}}{|\vec{r}'|} \quad (2.3)$$

where  $r'$  is the distance from the symmetric of  $P$  (in relation to the aperture plane) to a generic point of the aperture.

Applying the Green's theorem to  $G$  and  $U(P)$ , the Rayleigh-Sommerfeld diffraction equation can be obtained:

$$U(P) = \frac{i}{\lambda} \int \int_{S'} U(P_{s'}) \frac{|\vec{n} \cdot \vec{r}|}{|\vec{r}|} \frac{e^{-ik|\vec{r}|}}{|\vec{r}|} ds' \quad (2.4)$$

where  $s'$  is an infinitesimal surface on  $S'$  and  $P_{s'}$  is a point on the aperture.

What has been done so far is basically to solve the wave equation with the boundary conditions of the aperture.

The Huygens-Fresnel principle has been applied through the integral over  $S'$ , which stands for a super-position of plane waves.

Equation 2.4 is the exact solution of the problem posed in this section.

Another version of the Rayleigh-Sommerfeld equation, which is commonly used for its simplicity, can be obtained as follows.

Once the distance between the image plane and the aperture is fixed,  $\vec{r}$  becomes a function of  $(x - x_1)$  and  $(y - y_1)$ . In this case  $(x, y)$  is the position of  $P$ , on the image plane, and  $(x_1, y_1)$  is a generic point on  $S'$ .

The function multiplying  $U(P_{s'})$  in equation 2.4 can then be written as  $h(x - x_1, y - y_1)$ :

$$U(x, y, z) = \int \int_{S'} U(x_1, y_1) h(x - x_1, y - y_1) = (U_{s'} * h)(x, y) \quad (2.5)$$

and doing the Fourier Transform (FT):

$$A(\alpha, \beta, z) = H(\alpha, \beta, z) A(\alpha, \beta, 0) \quad (2.6)$$

It has been shown that the propagation, from the aperture to the plane  $z$ , can be easily done in the Fourier space. Now the new variable is  $H(\alpha, \beta, z)$ , the transfer frequency characteristic.

This particular form of the Rayleigh-Sommerfeld diffraction equation will be used in the analysis of the wavefront in the 5th chapter. Indeed, it will make the propagation faster to be computationally calculated but still preserving the precision of the exact form in equation 2.4.

## 2.1.2 Fourier optics

Even though equation 2.4 is the analytical solution we were looking for, the double integral makes the field  $U(P)$  difficult to calculate. At this point approximations are needed. The only variable that can be Taylor expanded in 2.4 is  $\vec{r}$ . If  $P$  is far enough from  $S'$ , the approximation can be already stopped at the second or even at the first order. These are the Fresnel and Fraunhofer approximations respectively.

Assuming the distance between  $P$  and the aperture to be big enough for both approximations, in equation 2.4 the factor  $|\vec{n} \cdot \vec{r}|/|\vec{r}| \simeq 1$  and  $\vec{r}$  can be written as:

$$\begin{aligned} |\vec{r}| &= \sqrt{z^2 + (x - x_1)^2 + (y - y_1)^2} = \\ &= z \left[ \underbrace{1 + \frac{x^2 + y^2}{2z^2} + \frac{x_1 x + y_1 y}{2z^2}}_{\text{Fraunhofer app.}} + \frac{1}{2} \left( \frac{x_1^2 + y_1^2}{z} \right)^2 + \left( \frac{y - y_1}{z} \right)^2 + \dots \right] \end{aligned} \quad (2.7)$$

Fresnel app.

Substituting any of the two approximations in equation 2.4, it can be shown that the field in the image plane is related to the field in the aperture by FT [13]. In particular:

$$\text{Fresnel app. : } U(x, y) \xrightarrow{\text{FT}} U(x_1, y_1) e^{-\frac{ik}{2z}[x_1^2 + y_1^2]}$$

$$\text{Fraunhofer app. : } U(x, y) \xrightarrow{\text{FT}} U(x_1, y_1)$$

For completeness, it has to be clarified that FT is done from the spatial to the spatial frequency domain:

$$x_1 \rightarrow f_x = \frac{x}{\lambda z} \quad \text{and} \quad y_1 \rightarrow f_y = \frac{y}{\lambda z}$$

In the Fraunhofer approximation the contribution of each plane wave is linear. This means that  $U(x, y)$  is a super-position of the family of straight lines emitted with an angle  $(x/z, y/z)$  through the aperture. When this condition holds, we say we are in the *far field*, otherwise in the *near field*.

There is a physical meaning behind the *near* and the *far field*: in the *near field* the nature of the plane wave depends on each portion of the source, whereas, in the *far field* it depends on the propagation medium and on the aperture shape.

The reader could think that the only way to reach the *far field* is to position the image plane really far from the aperture. Luckily, there is a smarter way to reach it. The *far field* can be seen in the focal plane of a lens, positioned after the aperture  $S'$ . Indeed, in its focal plane, a lens focuses the parallel rays, according to their angle with the

optical axis. As seen above, being the *far field* FT of  $U(P)$ , can be stated that a lens is Fourier transforming, in its focal plane, the field in the aperture.

This result represents a cornerstone of Fourier optics [14]. In our case, it brings two important consequences:

- 1- If the incoming beam is limited, the focus dimension would end up being “unlimited”, with the higher spatial frequencies further away from the brightest spot. Indeed, the FT of a limited domain has an unlimited domain. Anyway, this does not result in a big energy loss. For example assuming a circular aperture, the intensity in the focal plane will have a  $\text{sinc}^2$  distribution. The distance between two consecutive minima will be constant and the ratio between two adjacent peaks 1/25. Basically, all the energy will be enclosed in the Airy disk, which is defined as the region between the first 2 minima including the brightest peak [15].
- 2- The focal spot, which is the area within the highest intensity drops by half of its value, cannot be smaller than FWHM of the *Airy disk*. When this condition is valid, we say the system is diffraction limited.

The Airy disk size depends on the beam wavelength,  $\lambda$ , and on the numerical aperture of the focusing optics, NA, according to the relation:

$$d_{\text{Airy}} = \frac{\lambda}{2NA} \quad (2.8)$$

From equation 2.8 can be seen that once the wavelength is fixed, the only way to have a smaller spot is by increasing NA.

## 2.2 The off-axis achromatic aberration

### 2.2.1 The diffraction theory of aberration

Before describing the aberration, we need to introduce the concept of wavefront. The wavefront can be defined as the locus of points which connects the photons emitted at the same time from the same source. For example, a flat wavefront can be seen as the surface described by the photons with the same phase, emitted from a source set to infinity. This provides information about the energy direction propagation of the beam. Indeed, the Poynting vector is always perpendicular to the wavefront. As a consequence, the wavefront is not directly related to the beam propagation direction but rather to its energy flux.

The aberration is nothing else than a distortion in the wavefront and therefore in the optical ideal energy flux. To get a quantitative idea of the deformation induced by it, the following system will be taken into account:

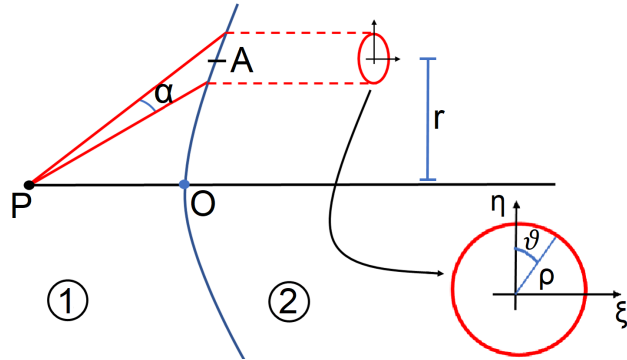


**Figure 2.2:** A beam, initially in the medium 1, passes an optical system, medium 2. The circle below is a zoom in of the beam profile in the medium 2.

In figure 2.2 a monochromatic beam (in red) with source  $P$  and aperture  $\alpha$  is initially in vacuum (1). It then propagates through an optical system (2) with a refractive index  $n$ . In (2) the beam profile is supposed to be a circle of radius  $\rho$ , perpendicular to  $\overline{PO}$ . The two axes perpendicular to  $\overline{PO}$  are called  $\eta$  and  $\xi$ , whereas,  $\vartheta$  is the angle between  $\rho$  and the positive semi-axis of  $\eta$ . As shown in figure 2.3, the deformation, induced by the aberration, results in a displacement of the wavefront from the ideal geometric one. We define  $a$  as the distance between ideal and real wavefront and  $b$  the distance between the ideal and the position where the ray falls in the image plane.

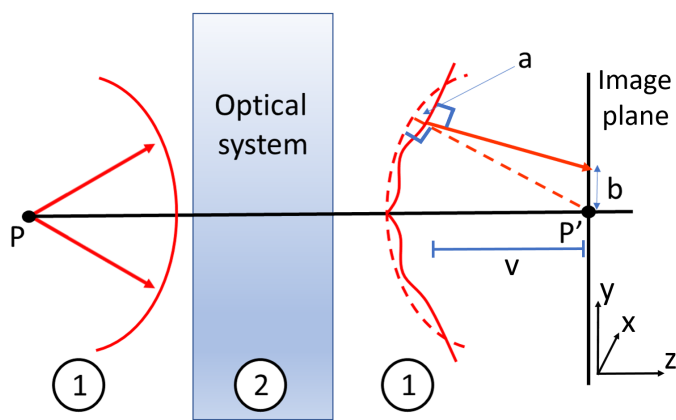


**Figure 2.3:** The beam in figure is affected by aberration, after leaving the optical system. The dashed lines represent the ideal beam path and wavefront, whereas, the continuous lines show the propagation due to aberration. [16]

Using just a single camera, the only visible quantity is  $b$ , as it can only detect intensities. It is not possible to directly display  $a$ .

Our aim is to find out the relation between  $b$  and the effect of aberration. Looking at figures 2.2 and 2.3, the values for  $a$  and  $b$  can be obtained as a function of the coordinate system parameters [16]:

$$a = k[\xi^2 + (\eta + r)^2]^2 \quad (2.9)$$

$$b = \sqrt{b_x^2 + b_y^2} \quad (2.10)$$

where:

$$b_x = \frac{v}{n} \frac{da}{d\xi} \quad (2.11)$$

$$b_y = \frac{v}{n} \frac{da}{d\eta} \quad (2.12)$$

In equation 2.9,  $r$  is the same as in figure 2.2, the distance between the centre of the optical system and the centre of the beam, when it enters the medium 2. In equation 2.10, the indexes  $x$  and  $y$  represent the axes, in the image plane, relative to  $\xi$  and  $\eta$  respectively. In equations 2.11 and 2.12,  $v$  is the distance from the image plane to the position in the wavefront where  $a$  is measured (see figure 2.3).

Writing  $a$  in terms of  $r$ ,  $\rho$ , and  $\vartheta$ , the following expressions for  $b_x$  and  $b_y$  can be obtained:

$$b_x = B\rho^3 \sin\vartheta - Fr\rho^2 \sin 2\vartheta + Dr^2 \rho \sin\vartheta \quad (2.13)$$

$$b_y = B\rho^3 \sin\vartheta - Fr\rho^2 (1 + \cos^2\vartheta) + (2C + D)r^2 \rho \cos\vartheta - Er^3 \quad (2.14)$$

In equations 2.13 and 2.14, the capital letters represent the different contributions to the total aberration, in particular:

B = Spherical aberration

F = Coma

D = Curvature of the field

C = Astigmatism

E = Distortion

The goal is to optimise the optical system in such a way that the aberration is reduced to the lowest value possible. This would diminish the focal spot area, increasing its intensity.

Correcting aberrations can either be done by changing the position of the optical components or adding an adaptive wavefront shaping element.

In a simple optical system, consisting of a single lens, a shift along the axis  $\overline{PO}$  would result in a piston (constant shift of the wavefront) or in a defocused picture. These variations do not really correct for aberration. Instead, a rotation of the lens around the axes perpendicular to  $\overline{PO}$  has a more interesting effect. Such influences have to be understood to achieve high intensity in the focus of the final focusing optics. These will be discussed in the 4th chapter.

As a last analysis, it can be interesting to estimate which difference is acceptable to consider the aberration negligible in a non ideal system. The usual parameter used is the “quarter wavelength of Rayleigh”. This states that if the difference between the ideal and the real wavefront is less than  $\lambda/4$  all over the wavefront, then the system can be considered ideal. This condition alone is not enough for most of the applications, wherefore, it is often imposed the continuity of the wavefront too [17].

### 2.2.2 The Zernike polynomials

As has been demonstrated in [18], one intensity distribution is not enough to retrieve all the different terms of the aberration. There is a degeneracy of solutions which results in a shift in the intensity distribution but not in a different shape. Writing down the normalized (to the ideal case) intensity distribution,  $i$ , the following is obtained:

$$i(P') = \frac{1}{\pi^2} \left| \int_0^1 \int_0^{2\pi} e^{ika} \rho d\rho d\vartheta \right|^2 \quad (2.15)$$

The highest value of  $i(P')$  is the so-called *Strehl ratio* and gives an idea about the strength of the aberration in the optical system. In particular, it quantifies the wavefront distortion, not being affected by intensity modulations.

Equation 2.15 can be easily solved by writing  $a$  as a set of orthogonal polynomials. A good choice of this set are the so-called Zernike polynomials,  $Z_p$ . These have rotational symmetry properties, which allow to separate the spatial from the angular dependency. Due to this feature,  $Z_p$  do not change their form even though the coordinate system is rotated by an arbitrary angle. Each polynomial has two variables;  $\rho$  and  $\vartheta$ , and two

parameters;  $n$  and  $m$ . The general form of  $Z_p$  can be written as:

$$Z_n^m = R_n^m \cos(m\phi + \frac{\pi}{4}[1 - (-1)^n]) \quad (2.16)$$

where  $R_n^m$  is the radial term and  $m$  and  $n$  are the azimuthal and radial order respectively. The description given by  $Z_p$  is valid only for rotationally symmetric systems. This means that if the beam is not circular symmetric,  $Z_p$  are not able to describe the different aberration contributions correctly [19].

## 2.3 The Gaussian beam

Now that the theoretical background has been discussed, the experimental set-up in the LION cave can be better understood. We want to analyse how the achromatic 90° off axis parabola (OAP), the final focusing optics, acts on a broad laser beam.

A parabolic mirror has the main effect of changing a flat wavefront into spherical. It is equivalent to state that the phase is parabolic in each plane.

This characteristic gives a first hint that the beam after OAP could be Gaussian. A further proof of this is given by the *sinc* amplitude distribution. Indeed, around the central peak, it approximates quite well a Gaussian profile. Actually, before OAP the ATLAS-300 intensity profile is well resembled by a super-Gaussian, which means that the Gaussian SID approximation in the OAP focus is acceptable and may even fit better than a *sinc*<sup>2</sup>.

Before studying the Gaussian beam in details, we need to introduce some basic quantities. These are reported below and in figure 2.4:

- $w(z)$ : is the *beam waist*. It is the radius of the circle, perpendicular to the beam propagation direction, where the intensity drops by  $1/e^2$ .
- $w_0$ : is the beam waist in the focal spot.
- $z_r$ : is the *Rayleigh length*, the distance from  $w_0$  to the plane with a beam waist of  $\sqrt{2}w_0$ . The physical meaning behind this quantity is the collimation <sup>1</sup> of the beam; the longer  $z_r$  the more collimated the beam is.
- $\vartheta_0$ : is the semi-aperture of the beam. It is the angle between the beam propagation direction and one of the asymptotes of the Gaussian beam profile.

---

<sup>1</sup>A beam is called collimated when  $w(z) = w_0$

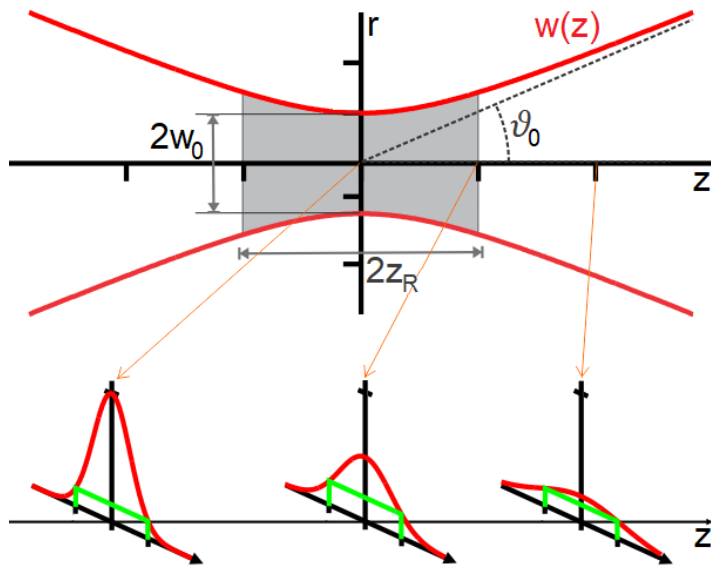


**Figure 2.4:** An ideal Gaussian beam results in a hyperbolic beam waist profile (in red). The beam propagation direction is parallel to the positive  $z$ -axis. The intensity distributions and the beam waist (in green) in the planes:  $z=0$ ,  $z_r$  and  $2z_r$  are shown below. Picture edited from [20].

The Gaussian beam can be defined as a particular solution of the Helmholtz equation 2.2. Taking into account a beam propagating in vacuum, the following can be stated:

- the energy flux is along the beam propagation direction
- the beam is cylindrically symmetric to its propagation direction

Assuming that the variation of  $\vec{E}$  along  $z$  can be well approximated by its first derivative,  $\vec{E}'$ , describing a Gaussian beam, can be written as:

$$\vec{E}(r, z) = \vec{E}_0 \frac{w_0}{w(z)} e^{-r^2/w^2(z)} e^{-ikr^2/2R(z)} e^{-i[kz - \phi(z)]} \quad (2.17)$$

where:  $r$  is the radius perpendicular to  $z$ ,  $1/R(z)$  is the curvature of the wavefront and  $\phi(z)$  is the Guoy phase shift. The last is a shift of  $\pi$  in phase, when the beam goes through the focus.

From equation 2.17 one can deduce that the Gaussian intensity profile is preserved not only at each  $z$  but also after a thin lens [21]. Also from the same equation, the phase in each plane can be obtained:

$$\varphi(r, z) = -i \left( kz + k \frac{r^2}{2R} - \phi(z) \right) \quad (2.18)$$

As expected, this is a parabolic function cylindrically symmetric to  $z$ .

A Gaussian beam can be fully characterized by its  $w_0$ , the only other dependency is the wavelength. Indeed, all the parameters defined at the beginning of this section can be written as a function of  $w_0$ :

$$z_r = \frac{\pi w_0^2}{\lambda}, \quad \vartheta_0 = \frac{\lambda}{\pi w_0}, \quad R(z) = z[1 + \left(\frac{z_r}{z}\right)^2]$$

A direct relation between the quantities above and the characteristics of the focusing optics can be obtained;  $\vartheta_0$  is equal to NA of the parabola.

The curvature of the wavefront can be derived from the third equation. It is zero at  $z=0$  and  $z = \infty$ .

Among the other beam shapes, the Gaussian beam has the highest intensity in the smallest spot, wherefore, it has the highest energy in FWHM. To demonstrate this, it is enough to have a look at the properties of FT. Indeed, there is a special link between its two domains, for example, in the temporal domain the relation is:  $\Delta t \Delta \omega \geq 2\pi$ , whereas, in the spatial domain:  $\Delta x \Delta k \geq 2\pi$ .

The Gaussian is the only function which minimizes both products and for this reason is the best candidate for the laser focus.

The importance of this characteristic and of the wavefront flatness at  $w_0$  will be explained in the next section, in the context of the laser ion-acceleration.

## 2.4 Laser-driven ion acceleration

So far the laser focus characteristics have been analysed. Now we are interested in studying how these affect the laser-driven ion acceleration.

Here, the acceleration process strongly depends on the laser intensity impinging on the target. Over the last decades, several different acceleration mechanisms have been defined, which are, upon other conditions, distinct by available peak intensity on target. Assuming a limited diffraction optics (see equation 2.8) and an energy of 2 J in FWHM on target, by focusing ATLAS 300 with an f/2 OAP, an intensity of  $8.57 \cdot 10^{21} W/cm^2$  is theoretically achievable. Due to aberrations and slight misalignments during the experiments, the intensity reached is on the order of  $10^{20} W/cm^2$ . This intensity brings our attention to two acceleration mechanisms: the Target Normal Sheath Acceleration (TNSA), which dominates between  $10^{18} W/cm^2$  and  $10^{20} W/cm^2$ , and the Radiation Pressure Acceleration (RPA), which dominates above  $10^{23} W/cm^2$  for a non circularly

polarized laser [11].

Both TNSA and RPA are "two-steps" acceleration mechanisms. First, the laser transfers energy to the electrons, which then in turn accelerate the ions. To reach a "one-step" process, where the laser directly accelerates the ions, the laser would need to have an intensity of  $10^{24} \text{ W/cm}^2$  at least.

The main idea behind the TNSA mechanism is now briefly explained.

The strong electric field of the laser is felt by the electrons in the surface facing OAP (the front size). The electrons which directly receive energy from the laser are called "hot" electrons. These are expanding along the beam propagation direction with a half angle of  $20^\circ - 45^\circ$ , fully ionising the target and generating a plasma. If the hot electrons are energetic enough, they can go through the target and leave the opposite surface (the rear side), generating a strong electric field normal to the positive left target surface. This electric field, which is of the same order of magnitude as the laser's ( $\text{MV}/\mu\text{m}$ ), can eventually rip off and accelerate the ions.

In this view, the role of the wavefront becomes clearer. We want that the plasma is ignited on the target at the same time by the entire focus. Indeed, a wavefront distortion would result in a non uniform  $\vec{E}$  on the rear side of the target, worsening the energy transmission.

Comparing the TNSA with the RPA regime, it can be shown that the ion energy scales with  $\sqrt{I_{\text{Laser}}}$  for TNSA, whereas, for RPA the dependency is linear. This means that tailoring the system to favour the RPA mechanism would also result in a more efficient ion energy-intensity dependence [1]. Furthermore, in TNSA the dominant accelerated ion species is the lightest element in the target, whereas in RPA there is not a dominant species. This makes the acceleration of heavy ions easier for RPA than for TNSA.

The reader can refer to [11] [1] for a detailed analysis of these two processes.

### 2.4.1 Plasma physics

The acceleration process does not only depend on the laser intensity. Two other important dependencies are the target damage threshold and the laser contrast. Before describing these dependencies, we need to introduce some basic concepts of plasma physics.

One of the elements with the highest ionisation energy is hydrogen. A laser needs an

intensity of  $\sim 3.51 \cdot 10^{16} \text{ W/cm}^2$  to ionize it.

Nevertheless, a laser intensity of  $10^{12} \text{ W/cm}^2$  is already high enough to melt or to fully ionise most of the solid targets. The ATLAS-300 peak intensity,  $10^{20} \text{ W/cm}^2$ , is more than sufficient to generate a plasma when a thin foil is positioned in the OAP focus. We talk about *plasma* when a medium is partially ionised but globally neutral and shows collective behaviours. The last ones are due to the electromagnetic interaction between both different and same species (ions and electrons). A consequence of these characteristics is that the electric field inside the plasma is zero. It behaves like a conducting material. Therefore, if an external charge is placed in the plasma, the free charges rearrange such that  $\vec{E}$  inside is still zero on scales of the Debye length,  $\lambda_D$ . The last is the distance after which an external electric potential drops by  $1/e$ . The Debye length allows also to define the following “plasma approximation”. If the number of charge carriers in a sphere within a radius of  $\lambda_D$  is much higher than one, we say that the plasma shows collective behaviours. Indeed, in TNSA, it is no coincidence that in the rear surface  $\vec{E}$  scales with  $1/\lambda_D$  if  $d < \lambda_D$  and with  $1/d$  if  $d > \lambda_D$ . We called  $d$  the distance between the electron layer and the rear surface.

If a short single electric pulse is applied to a plasma, basically only the electrons are displaced. Indeed, as electrons are three orders of magnitude lighter than protons, the ions can be considered as a fixed background. After the short pulse, the electrons oscillate in the electric field  $\vec{E}$ , generated by this displacement. The frequency of this oscillation is called plasma frequency,  $\omega_P$ .

The following relation links  $\lambda_D$  to  $\omega_P$ :

$$\lambda_D \omega_P = v_{th} \quad (2.19)$$

where  $v_{th}$  is the thermal velocity of the electrons.

As  $\omega_P$  is not directly depending on the temperature, the higher  $v_{th}$  the higher  $\lambda_D$ . According to the analysis done above, a higher  $\lambda_D$  results in a more stable  $\vec{E}$  in  $d$ . This means that the higher the electron temperature, the more efficient the ions acceleration. In other terms, the laser has to be able to transfer the highest energy possible to the electrons.

## 2.4.2 Damage threshold and laser contrast

The laser can transfer its energy to the plasma as long as absorption is possible. This energy absorption does not happen as long as the electron density,  $n_e$ , is higher than the critical density,  $n_c$ :

$$n_c = \frac{m_e \varepsilon_0 \omega^2}{e^2} \quad (2.20)$$

The equation above can be obtained writing down the refractive index of the plasma. This is imaginary only if  $\omega_P > \omega_{Laser}$ . In this case, the plasma becomes over-dense and reflective for the laser.

To give the reader a magnitude to this quantity, for ATLAS-300 ( $\lambda = 800\text{ nm}$ ),  $n_c$  is in the order of  $10^{21}\text{ cm}^{-3}$ .

To use the full laser power, the plasma does not have to be reflective before the arrival of the main pulse. To fulfil this condition, the temporal evolution of the laser intensity has to be as steep as possible. This quantity, called *laser contrast*, is an important parameter that has to be measured and improved before shooting on thin foils.

As said in the section 2.4.1, the plasma expansion starts already when the laser intensity reaches  $10^{12}\text{ W/cm}^2$ . If below  $10^{10}\text{ W/cm}^2$  the target is just heated up, between  $10^{10}\text{ W/cm}^2$  and  $10^{12}\text{ W/cm}^2$  the electrons are already dissociated from the nuclei but not accelerated yet. The electron acceleration plays a role when the laser reaches an intensity higher than  $10^{18}\text{ W/cm}^2$ , basically, when these are relativistic.

If the laser contrast is not sufficient, the plasma could already have expanded such that most of the electrons are too far away to be directly accelerated by the laser when it reaches the intensity of  $10^{18}\text{ W/cm}^2$  [22]. Furthermore, to increase the performance of TNSA, the target rear side should not be altered and be as flat as possible. This allows to define a threshold over which the target damage is irreversible, the *damage threshold*. For RPA this parameter is even more crucial, indeed, RPA would need both sides of the target undisturbed when the highest intensity is reached.

The *damage threshold* also influences the choice of the target material and thickness. As demonstrated in [23], a thinner target not always results in higher ion energies. A possible explanation for this could be, that below a certain thickness, the damage threshold is so low that the laser contrast is not good enough to accelerate the ions. Laser contrast measurements at ATLAS-300 have been made with two different third-order auto-correlators; Sequoia and Tundra. One of the measurements is shown in figure 2.5. Here, the main pulse is set to be at the time 0. It can be immediately

noticed that before the ramp up to the main pulse (in figure 2.5 between -100 ps and 0 ps), there are two spikes above the damage threshold. These pre-pulses can damage the target before the arrival of the main pulse. To get rid of them, in ATLAS-300, the settings of a Pockels cell (a fast optical shutter) have been changed.

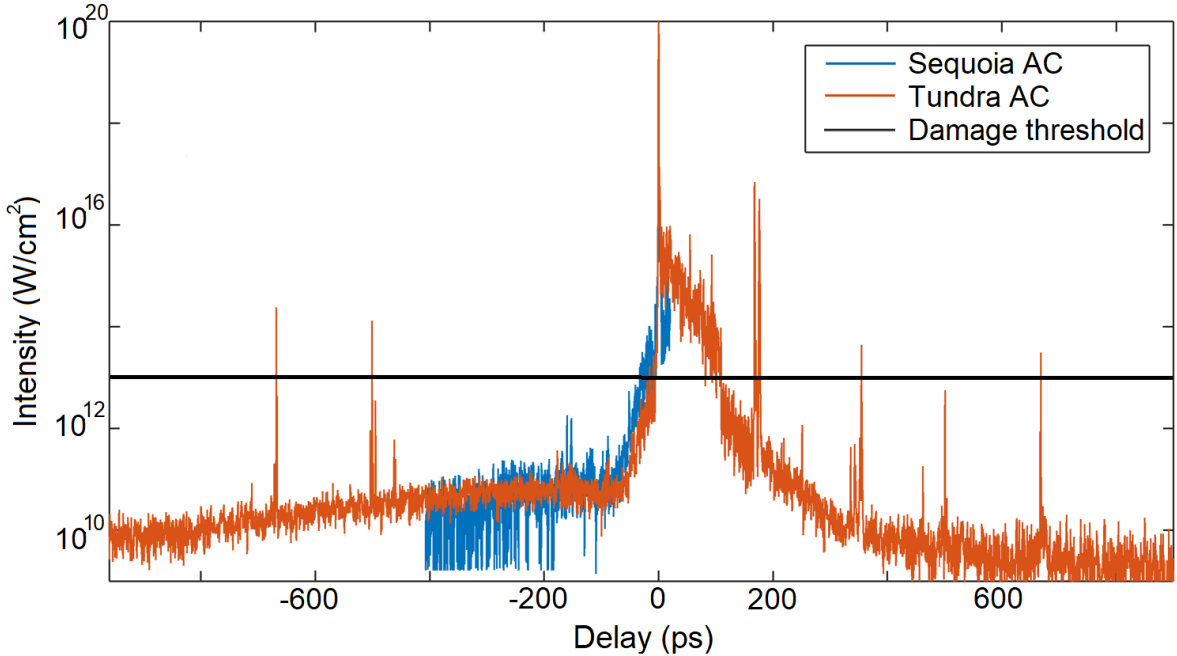


**Figure 2.5:** In blue the measurement done with Sequoia, in orange the one done with Tundra (a version of Sequoia with a longer temporal scanning range) and in black the damage threshold. To not damage the auto-correlators, the measurements have to be done with a low energetic version of ATLAS-300 [24].

### 2.4.3 Optical probing

The measurements taken with the auto-correlators are mainly limited by two factors:

- 1- the results are obtained from a significantly attenuated version of the beam
- 2- the results do not take into consideration effects of propagating from the compressor through the beamline to the target chamber

To overcome these limitations, an optical probing set-up has been developed in the side chamber of the LION cave [25].

The optical probing is based on the pump-probe technique. The pump is the main pulse, which is triggering the plasma expansion, and the probe is a small portion of the

main pulse, picked up when the main pulse enters the experimental vacuum chamber. The probe goes through a motorized delay stage, a chirping glass rod and then the interaction point between the main pulse and the point of the laser-target interaction, the so-called TCC (Target Chamber Centre). The delay stage is used to vary the time between the main pulse and the probe. The chirping rod, which stretches the pulse from 25 fs to few ps, allows to analyse the plasma expansion on a longer time scale. In TCC, when the plasma is over-dense, the probe cannot go through. After TCC, following the probe propagation direction, what we expect to see is a shadow where and when the plasma was reflective. Because of the chirp, the longer wavelengths of the probe will see the plasma expansion at an earlier stage compared to the shorter wavelengths. Basically, the information about the plasma expansion is embedded in the different wavelengths of the chirped probe. The last step is to convert this information from the frequency to the time domain. Applying a technique also used in [26], nine spatially separated replicas of the probe are created by a grating multiplier. Different bandpass filters, positioned in a 3x3 matrix, select different portions of the replicas, which are finally detected by a camera. The final result is a picture displaying nine frames of the plasma expansion in a time window of 1 to 7 ps (based on the length of the chirping rod). From these pictures the normalized (to the damage threshold) contrast curve can be retrieved on-target with 2 methods, by:

- 1- studying the plasma expansion
- 2- varying the laser energy

Both methods allow to have, for the first time, an on-target measurement of the temporal intensity distribution of a high-power laser. Using the first method, it is possible to retrieve the normalized contrast curve in a single shot mode. Instead, the second method allows the same but requires more than one shot.

For further details about the optical probing the reader could refer to [25].

Thanks to this technique, it is also possible to have a direct information about the plasma expansion and the spatial intensity distribution. The latter will be the topic of the next chapter.

# **3 The laser focus spatial intensity distribution**

The importance of temporal laser contrast has been analysed in the last section of the previous chapter. This quantity alone is not sufficient to define the quality of the laser focus. SID is another crucial parameter which has to be characterised too. Indeed, a complete knowledge of this would result in a more precise calculation of the energy within FWHM.

This is a key factor, which is usually calculated using a single picture.

In the experiments done at ATLAS-300 in the LION cave, the ion energies were lower than expected, indicating that the energy enclosed in FWHM could have been overestimated. A possible solution to this problem will be presented in this chapter.

The importance of the laser SID will be stressed in the first section. In the second, a characterisation of a logarithmic CMOS camera will be exposed. In the last one, the possible applications of the logarithmic camera and its pixel scheme will be discussed.

## **3.1 High dynamic range focus pictures**

For the reasons explained in the 2nd chapter, to obtain high ions energies, the laser energy enclosed in FWHM has to be the highest possible.

A direct way to get a feeling of the focus quality is to use a photo-sensitive device, for example, a camera chip.

In the LION beamline, the laser focus is imaged by a microscope on two CMOS cameras; a high magnification, High Mag (20x), and a low magnification camera, Low Mag (5x). Both are 10 Bit cameras with a Dynamic Range (DR) of 62 dB. A drawing of the microscope used in the LION main chamber can be found in figure 3.1.

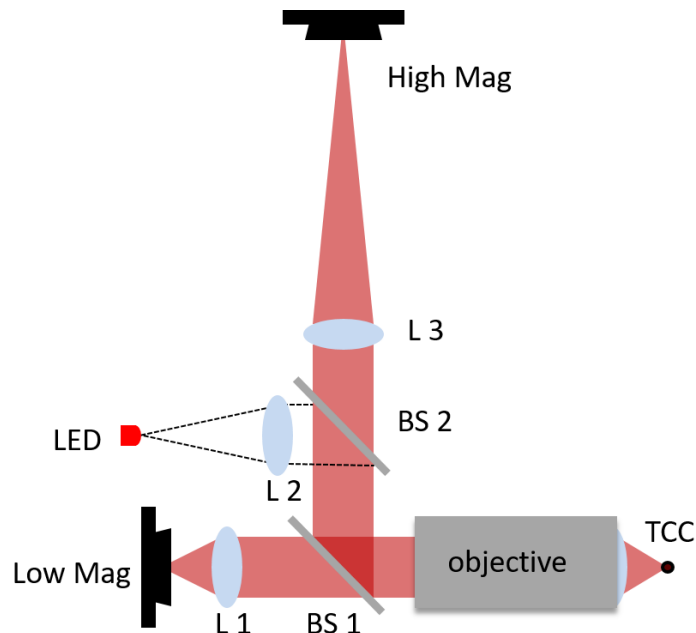
To fully analyse the focus, several images with rising intensity levels have been recorded. These have been obtained by changing the laser filter settings before the compressor. A complicated analysis of these focus pictures leads to a High Dynamic Range (HDR)

image. An exemplary taken HDR focus picture of ATLAS-300 in the LION side chamber is shown in figure 3.2. It reveals a narrow peak and a broad lower intensity region. Even though the intensity of the outer region is lower, it contains a significant portion of the energy and thus influences the focus analysis severely.

For a quantitative analysis of this effect the reader can refer to [24].

The broad region has an intensity around three Orders of Magnitude (OM) lower than the peak. This means that a camera needs more than three OM to correctly calculate FWHM in a single picture. DR of the cameras mentioned above is not high enough to detect both the broad region and the peak. Indeed, of the six OM theoretically available, less than three can be reached within one picture.

It is not possible to retrieve a full characterisation of the focus in a single picture. Therefore, more pictures need to be acquired, to fully reconstruct a HDR SID. Due to the laser jitter, achieving spatial overlap is the main source of error in the HDR pictures. The only way to reduce this error is to use a camera with an intrinsically high enough DR. The characterisation of such a camera (from now on called: HDR camera) will be the topic of the next section.



**Figure 3.1:** The picture shows a sketch of the microscope used in the main and side LION chamber. L stands for lens and BS for beam splitter. Picture edited from [25].

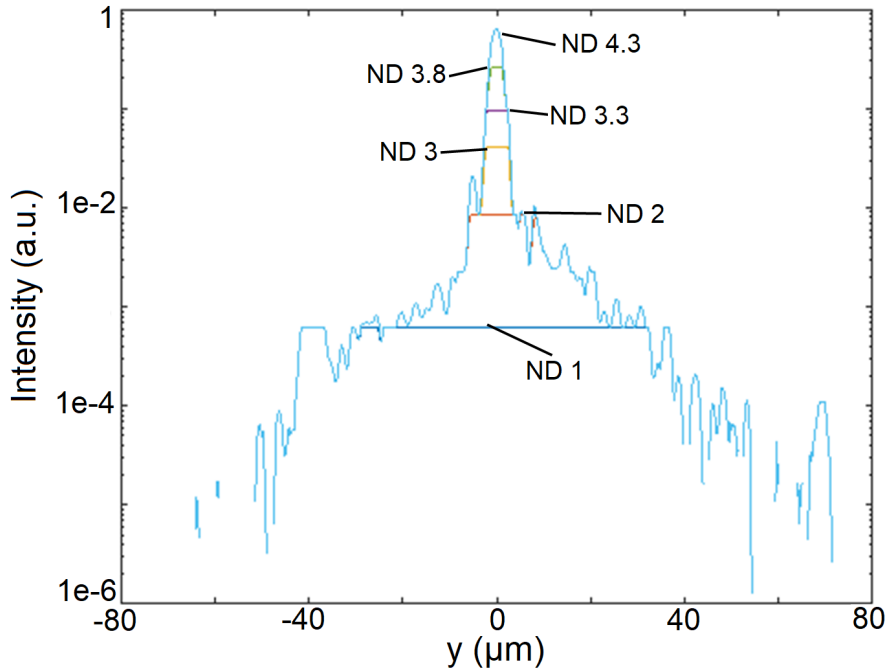


**Figure 3.2:** Reconstruction of an HDR focus of ATLAS-300 in the side chamber. The normalised intensity values are shown as a function of a spatial coordinate, perpendicular to the laser direction. The horizontal lines represent the highest intensity recorded for a given Neutral Density (ND) filter setting. The distribution clearly gets wider between ND1 and ND2. Picture edited from [25].

## 3.2 Camera characterisation

The alleged twelve OM are the main reason behind the characterisation of the CMOS camera UI-5120SE-M-GL. Its 120 dB would be more than sufficient to display the different regions of SID in a single frame. The features of this camera, provided by iDS, in which we are mainly interested, are:

- Sensor → CMOS Logarithmic
- Shutter → Rolling shutter
- Readout mode → Progressive scan

A complete data sheet can be found in [27].

The first step is to understand if these characteristics allow a quantitative analysis of our laser focus. To fully characterize the HDR camera, four tests have been done. During these tests the pixel clock value has been set to 31 MHz, the highest allowed by the software. To test the camera, the set-ups in figures 3.3 and 3.4 have been used;

**1st and 2nd test: Light source → LED**

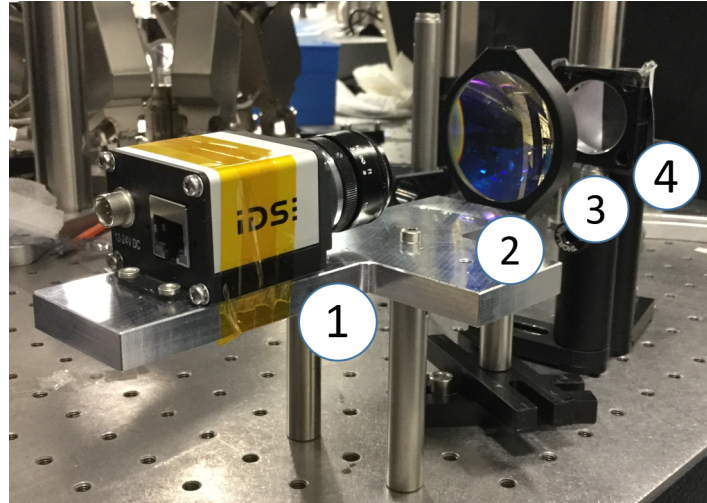


**Figure 3.3:** (1) HDR camera, with an objective. (2) Lens, used to image the grey-scale pattern in the camera chip. (3) Grey-scale pattern, to have both over and under exposed regions in a single exposition, see figure (c) first test. (4) Green LED.

**3rd and 4th test: Light source → Greeny <sup>1</sup>**

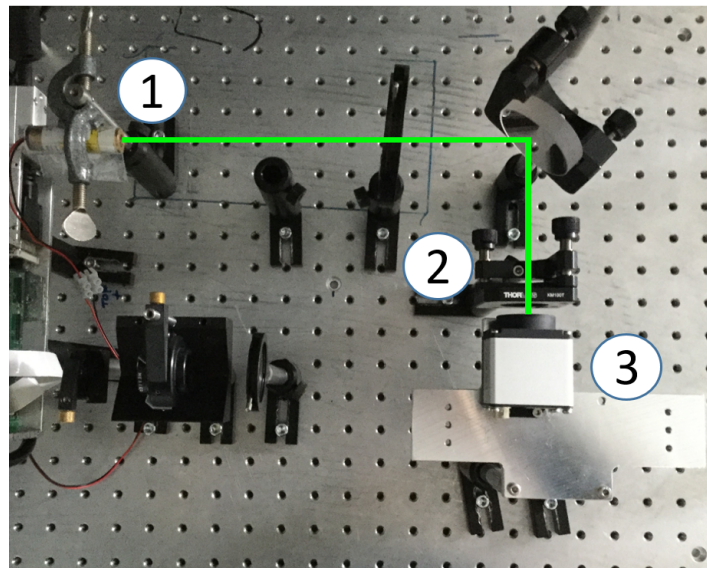


**Figure 3.4:** (1) Greeny, 532nm wavelength. (2) Slit, 15  $\mu\text{m}$  aperture. (3) HDR camera. The distance between the slit and the HDR camera has been optimized to image only the 0th, the 1st and 2nd order maxima.

---

<sup>1</sup>A solid state green laser pointer.

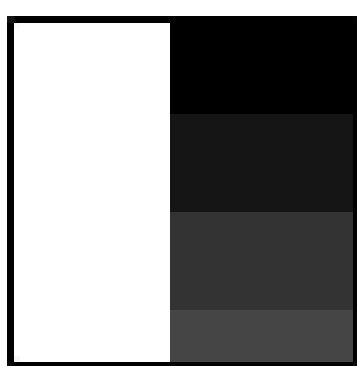
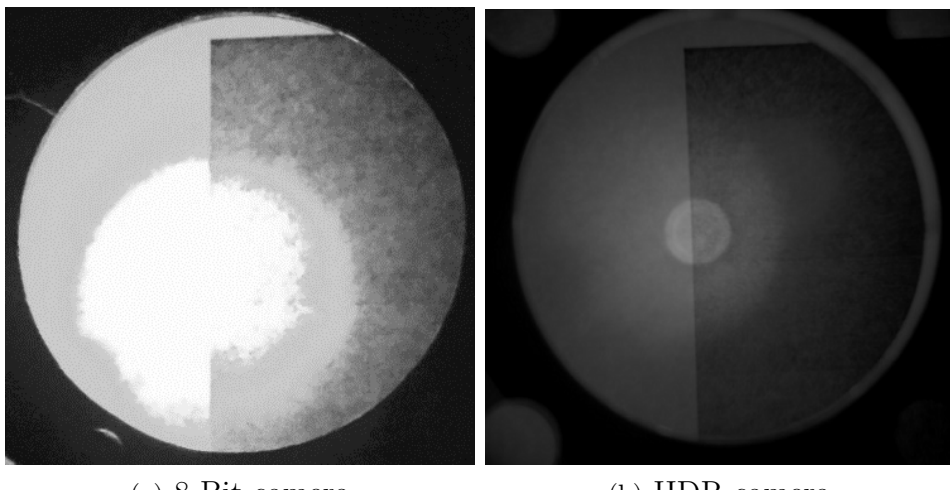
## Comparison between an 8 Bit and the HDR camera (first test)

**Goal:** Get a qualitative idea of the camera DR.

**Settings:** Both LED and the HDR camera in free-run mode.

**Procedure:** Compare the HDR camera to an 8 Bit camera by imaging the same grey-scale pattern.

The results are shown in the pictures below:



(c) Original grey-scale pattern

**Figure 3.5:** In (a) and (b) the pictures obtained with the devise written below these. In (c) the grey-scale pattern imaged in the camera, in figure 3.3 number 3.

The HDR camera can resolve the different exposed regions and the lines between them are visible too. The lack of saturation in the HDR camera is due to its logarithmic behaviour.

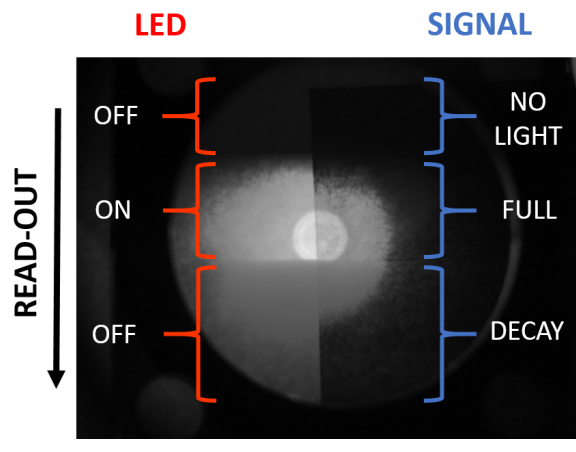
## The HDR camera reading process (second test)

**Goal:** Understand the reading process of the HDR camera and if it can be used to image fast events.

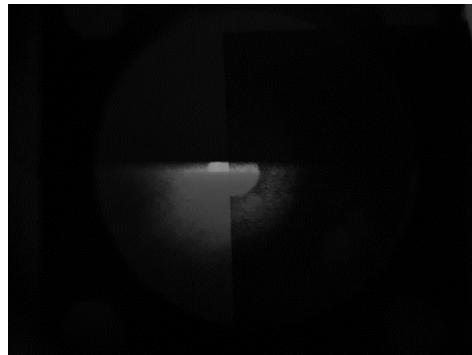
**Settings:** Both LED and the HDR camera in trigger mode.

**Procedure:** Connect LED and the HDR camera to the same trigger. Compare the pictures recorded with increasingly shorter pulse durations (p.d.)<sup>2</sup> of LED to the intensity detected by a photodiode.

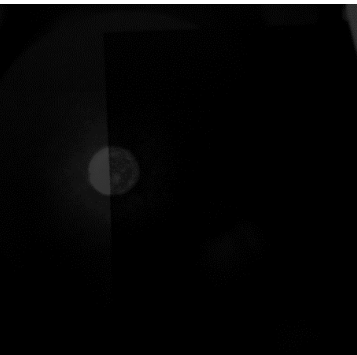
The figure below shows the pictures obtained. They have been taken with a trigger frequency of 2.5 Hz and with p.d. defined below each picture:



(a) P.d. 10 ms



(b) P.d. 1 ms



(c) P.d. 0.1 ms

**Figure 3.6:** The three pictures show the frames taken with three different LED p.d. In the first one, (a), is displayed the evolution of the signal (blue brackets), as a function of the LED state (red brackets).

---

<sup>2</sup>Pulse duration: Interval of time in which the voltage on LED is above 80% of its maximum value.

Looking at pictures (a) and (b) in figure 3.6, the different LED stages are clearly distinguishable from top to bottom. Before LED is *off* (top dark part, *no light*), then *on*, for a duration given by p.d. (brightest central part, *full*) and, finally, *off* again (low grey part, *decay*). The event in picture (c) is already too fast to distinguish the stages mentioned above.

It is the *rolling shutter effect* which creates a sequence of events in a single frame. This is an artefact due to the continuous read-out of the chip, in our case from top to bottom.

From the known p.d., the total read-out time can be calculated to be 36 ms. This does not mean that the only recordable events need to last longer than this value. Indeed, the initial intensity could be retrieved from the decayed signal (low grey part). Our new goal is to find out the decay law.

A direct correlation between the LED signal and the one read by the camera is now needed. For this reason, a photodiode has been positioned between the lens and the grey-scale pattern (in the set-up figure 3.3 (2) and (3) respectively). The comparison is reported in the figure below:

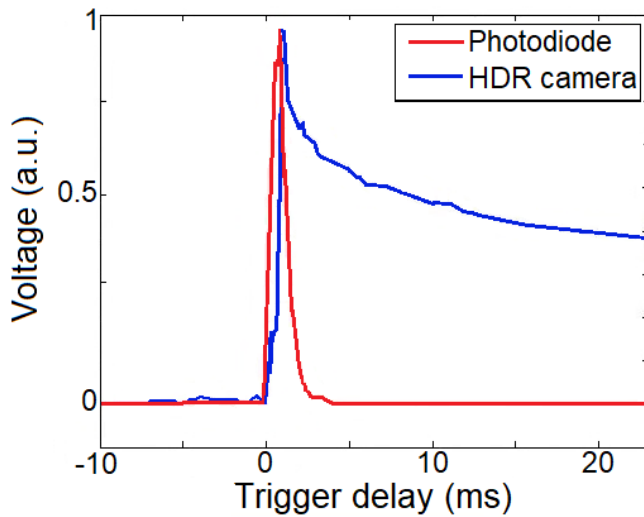


**Figure 3.7:** Comparison between the photodiode and the HDR camera signal. The blue line is the integrated signal over a line-out. This curve has been obtained changing the trigger delay between LED and the HDR camera.

The signal decay seems to follow a well defined trend. What is not known is the intensity dependence of this decay. This will be characterised in the third test, using a diffraction pattern.

## HDR camera tested with a known SID (third test)

**Goal:** Give a quantitative description of the camera read-out process.

**Settings:** Both the Greeny and the HDR camera in trigger mode.

**Procedure:** The Greeny impinges on a thin slit. A diffraction pattern is created and recorded by the HDR camera. The intensity distribution of the pictures is then compared to the theoretical result.

A diffraction pattern has been used to study if the signal decay of the HDR camera is intensity dependent. This provides an absolute intensity distribution reference, which can be compared with the frames taken by the HDR camera. A p.d. of 10 ms has been set. The frame is reported in figure 3.8. As expected, the rolling shutter effect is again visible and consequently the signal decay.

As known from the 2nd chapter, the theoretical value for the ratio between the first and the zeroth maximum is roughly 1/25. The same quantity can be calculated, for the HDR camera, taking a horizontal line out of the picture. To study the signal decay, wherefore, it is enough to plot this ratio as a function of the pixel line. The results are reported in the figures below. Furthermore, we expect the ratio between two maxima of the same order to be one. This ratio has been plotted in figure 3.9.

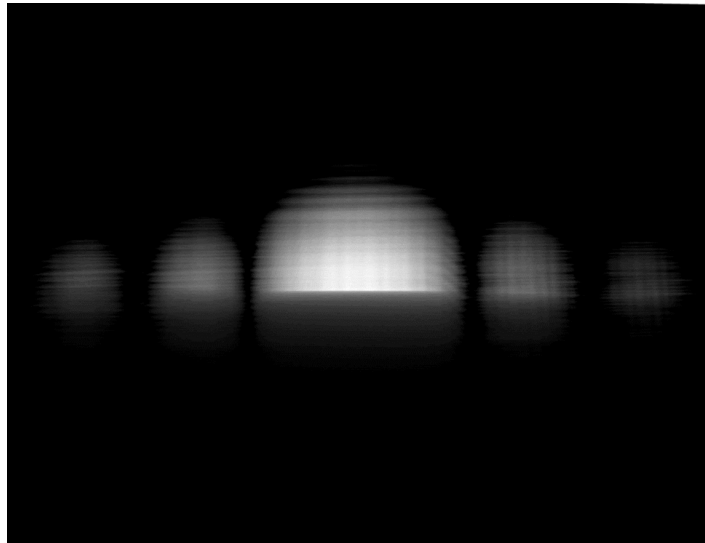


**Figure 3.8:** Frame whom the plots below are referred to.

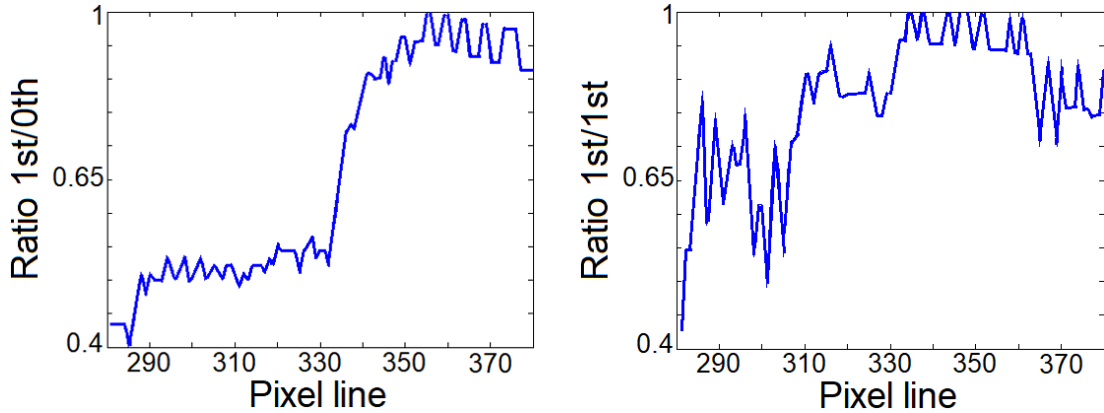


**Figure 3.9:** On the left plot, the ratio between the left first order and the zeroth maximum. On the right plot, the maximum intensity of the first order maximum, the one on the left of the maximum, over the one on the right.

The increase of the ratio in the plot on the left of figure 3.9, around the pixel line 330, corresponds to the decrease in intensity of figure 3.8. The ratio increases when the signal decays. In other terms, the signal decay is intensity dependent.

Anyway, the logarithmic characteristic clearly emerges, indeed, before the pixel line 330, the ratio is roughly 1/2. This is more than twelve times higher than the theoretical value.

The plot on the right shows big variations from line to line (in linear scale  $\sim 10\%$ ). The last aim is to discover what is the source of this instability.

## Source of the HDR camera artefacts (fourth test)

**Goal:** Understand if the instability in the data comes from the HDR camera read-out process or from the laser.

**Settings:** The Greeny in free-run mode and the HDR camera in trigger mode.

**Procedure:** Same procedure of the third test.

The small cavity of the Greeny not only needs a minimum voltage to work properly but also a minimum pulse duration. To test if the rise and the fall time of the Greeny is responsible for the strange behaviour, the laser has been set in free-run mode and the HDR camera in trigger mode. The results are shown below:

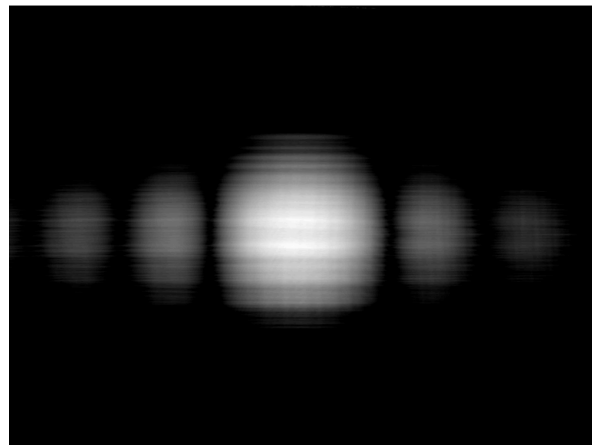


**Figure 3.10:** Frame analysed. The rolling shutter effect is not visible.

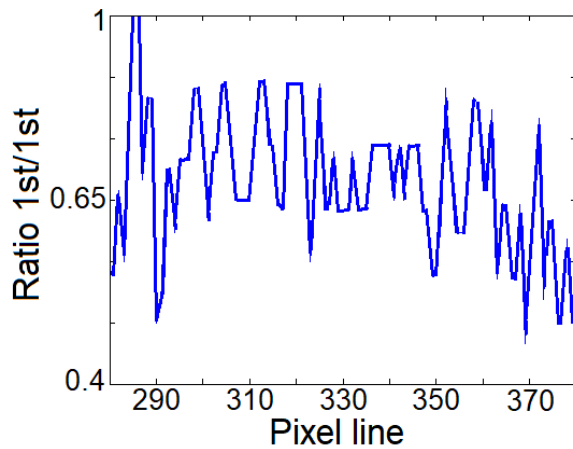


**Figure 3.11:** Maximum intensity of the first order maximum, on the left, over the one on the right, as a function of the pixel line.

The ratio in the plot above is still really noisy. The data are varying as the one obtained in the third test, in the not decayed region. This means that the variations are due to the HDR camera itself.

The similarities of the noise pattern in figure 3.9 (right plot before the signal decay) and 3.11 would suggest that each pixel has its own intensity dependent behaviour which does not change when excited. A further proof of this is represented by the pixel structure, which will be shown in the next section.

## 3.3 Overview and issues

### 3.3.1 The pixel-scheme

A deeper look at the structure of the pixel sensor is necessary to understand the reasons of the behaviours exposed so far.

The pixel sensor works with a three transistors (3T) logarithmic technology. The main difference, between the sensor of the HDR camera (logarithmic) and a linear sensor, is the lack of a reset pin. The two pixel-schemes are reported below:

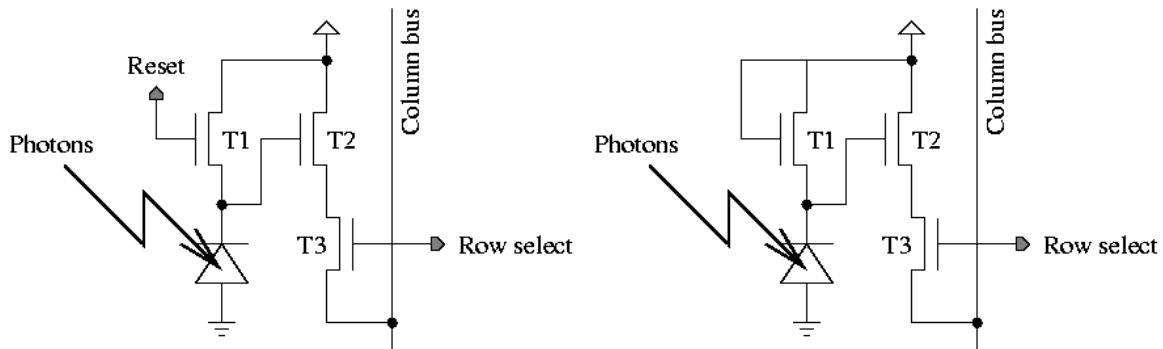


**Figure 3.12:** Linear and logarithmic pixel-scheme, respectively on the left and on the right. Pictures taken from [28].

In a logarithmic pixel, the first transistor (T1) works in a sub-threshold behaviour. This is the reason why the signal collected cannot be stored but it is continuously decaying. The transistor T1 is always on. In this regime, the resistance of the transistor depends on the voltage. This is what creates the logarithmic voltage response. The lack of a reset pin is both the strength and the weakness of the logarithmic-pixel.

### 3.3.2 Results and further applications

The main goal behind each test was to obtain a linear read-out scale from the measured signal. In this way, the focus characteristics could have been retrieved directly. The results shown in the different tests proof that this log-linear conversion cannot be easily calculated. The pixels show a different intensity dependence for both read-out and decay. Either the characterisation of each pixel would be needed or, assuming equal behaviour of each pixel, the characterisation of a pixel response to different intensities. During the investigation of the camera another strange behaviour has been noticed.

Even with fixed trigger delay and constant parameters the read-out was changing. The pixel line, where the signal starts decaying (see figure 3.6), changes from picture to picture. Even if the log-linear conversion curve would be known, it is not possible to correctly set its offset value.

Furthermore, the chip appeared really insensitive to bright sources. This makes the HDR camera damage threshold easily achievable, making its usage to a high-power laser very unfavourable. Anyway, the camera could be used to have a qualitative idea of slower events with a high brightness contrast. Whereas the 25 fs of the laser pulse are too short, the light emitted by a scintillator could be easily recorded.

The low sensitivity and the fast signal decay are clearly the main issues related to this HDR camera. A log-camera with a less steep decay time could be the best solution to make the retrieval of the signal feasible also for fast events.

# **4 A semi-automatic focus adjustment procedure**

The quality of the laser focus plays a significant role for the laser ion acceleration, as explained in chapter 2. For the development of a more reliable ion acceleration system, a controlled and reproducible focus alignment procedure is thus required.

In the first part of this chapter the shape of OAP and the characteristics of the Hexapod, a special positioning system, will be explained. In the second a LabVIEW program and its future developments will be presented. The program has been tested in the Medical Physics laboratories in Garching bei Muenchen and it will be used for the alignment routine in the new laser facility of CALA.

## **4.1 The 90° OAP**

In the LION cave the laser focus is obtained using an achromatic 90° OAP. This is a special mirror which has a peculiar shape, it is a portion of a 3D parabola, so-called mother parabola (see figure 4.1).

In such a 3D parabola the directrix is a plane and the focus is a spot.

The so-called off axis angle is the designed angle between incoming beam and the axis going through the parabola center and the focus point of the mother parabola.

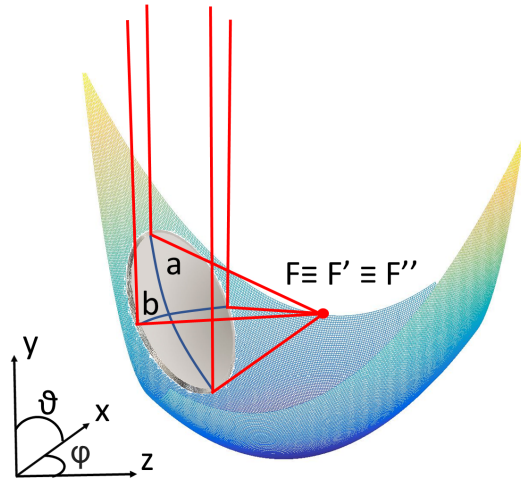


**Figure 4.1:** The main OAP axes are indicated with  $a$  and  $b$ .  $a$  is a section of a 2D parabola and  $b$  of a circle parallel to the directrix. Both  $a$  and  $b$  pass by the OAP centre. Though curved, they will be approximated straight.

In figure 4.1  $F$  is the 3D parabola focus,  $F'$  the focus along  $b$  and  $F''$  along  $a$ . These three points overlap if the beam is perfectly aligned and not affected by aberration. Assuming a perfect OAP and a flat wavefront, a misalignment before OAP could only cause an aberration in the focus. Referring to the System Of Coordinates (SOC) drawn in figure 4.1, a beam could be misaligned in two ways; rotated by  $\delta\vartheta$  towards  $x$  or towards  $z$ . Any other misalignment is just a combination of those two. An example is shown in the figure below:

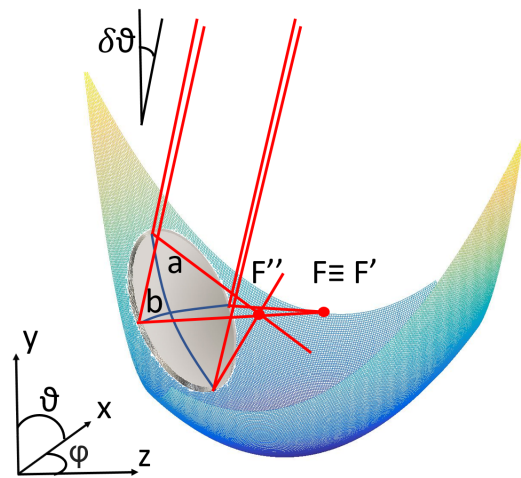


**Figure 4.2:** The case of the misalignment by  $\delta\vartheta$  towards  $z$  is shown.

In the ideal case of a Gaussian beam, the focus should have a circular beam waist with a Gaussian intensity distribution. Instead, the focal spot of figure 4.2 will be elliptically shaped with the ellipse axes parallel to  $a$  and  $b$ . The three foci of figure 4.1 do not overlap anymore,  $F''$  is closer to the OAP centre than  $F'$  and  $F$  ( $F'' \not\cong F' \cong F$ ). The beam in figure 4.2 is affected by vertical astigmatism. To correct for it, OAP has to be rotated around  $b$  until  $F'' \cong F$ .

The other case of misalignment happens when the beam is bended by  $\delta\vartheta$  towards  $x$  ( $F' \not\cong F'' \cong F$ ). The beam will still have an elliptical section. This time it will be rotated by  $45^\circ$  compared to the ellipse of the previous case.

The beam is affected by oblique astigmatism. To correct for it, OAP has to be rotated around  $a$  until  $F' \cong F$ .

In both cases of misalignment the ellipse axes are not fixed in length, they get swapped when going from  $F'$  to  $F''$ . This implies that there will be at least one point along  $z$ , between the two foci, in which the beam looks round shaped. This spot will be bigger than the one obtained when the three foci overlap. Apart from the planes just mentioned, the beam will look elliptically shaped. Therefore, the beam shape has to be checked in the planes close to the round shaped profile to visualize if it is astigmatic or not.

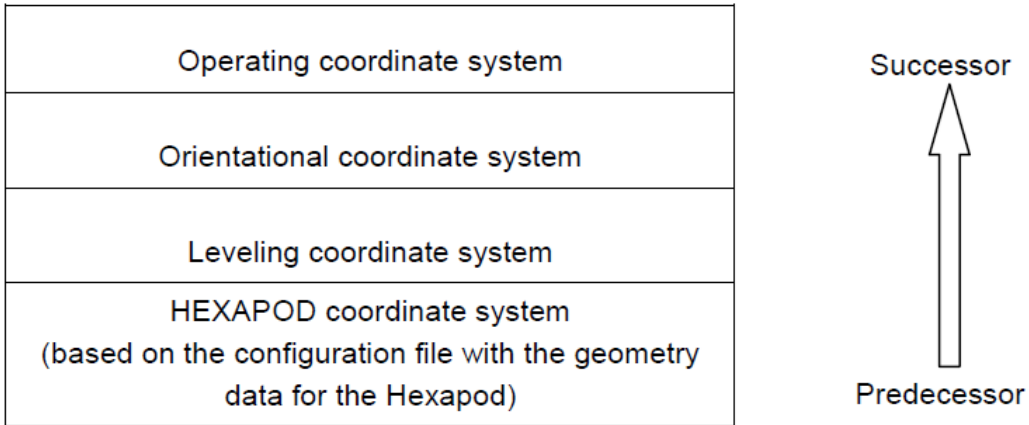
It has to be mentioned, for completeness, that a rotation around  $\varphi$  does not make any sense. Indeed, the incoming beam is cylindrically symmetric around  $y$ .

## 4.2 OAP positioning system; the Hexapod

The corrections mentioned in the previous section can be applied only if OAP is mounted on a precise positioning system. This needs to be vacuum compatible and have a high accuracy to be used during the experiments. In the previous experiments OAP was mounted with five motorised axes. As a compact solution a Hexapod is now used in CALA.

A Hexapod is a micro-robot, made of two circular plates and six motorised pistons. The bottom plate is fixed, instead, the upper plate can be moved by the pistons. The upper plate allows an object positioned on it to have six degrees of freedom (DOF). These are the same DOF of  $\mathcal{R}^3$  (the 3D Euclidean space), three translations and three rotations around each axis. In this way, it is possible to define a unique representation of a 3D rigid body in space.

The Hexapod software, provided by PI, allows to define different SOCs according to the following hierarchy:



- *HEXAPOD SOC*: it contains the specifics of the Hexapod model. This SOC is fixed by default.
- *Leveling SOC*: it takes into account for slight misalignments in the Hexapod positioning.
- *Orientational SOC*: it takes into account for the directions and the orientations of the axes.

Here it is defined the *ZERO SOC* which is the absolute starting position for each SOC. Its origin is at the centre of the bottom surface of the upper plate but it does not move with it.

All the *Orientational SOCs* are right-handed by default.

- *Operating SOC*: these are SOCs in which the user can directly operate. Here one has the possibility to define two SOCs; the *Work SOC* and the *Tool SOC*. The first one is fixed in space, instead, the second moves with the upper plate. The position of the *Tool SOC* is relative to the *Work SOC*, which is in turn relative to the *ZERO SOC*.

A clarification needs to be done: the systems defined so far are not exactly SOCs but rather *frames*. A *frame* is an extended definition of SOC. In  $\mathcal{R}^3$ , SOC is defined by three vectors perpendicular to each other (called *basis*). In the definition of *frame*, in addition to the basis, is also included one reference point. In our case this point is the

centre of rotation, the so-called “*pivot-point*” (PP). This is automatically defined for each SOC by the software. PP is always the origin of the *Tool SOC*.

As a consequence of this property, PP is not fixed in space but it translates with the upper plate. Instead, a rotation of the upper plate does not change either PP and the *Tool SOC* position.

In the experiments done so far, PP was set in the centre of the bottom surface of the upper plate (default choice given by the software). This is not the wisest solution as it has been shown in the previous section. To correct for astigmatism the rotation has to be done around the OAP main axes. For this reason, PP will be set in the OAP centre reflecting surface in the next beam-times.

Once fixed PP and two rotational axes, we have to define the translating ones. The need to scan the focus to check its shape brings to a natural choice of the axis  $z$ . It is the axis passing through the centre and the OAP focus. To define the other two axes, it is necessary to look at TCC. Taking into account the case of a rotation around  $a$ , the position of the focus relative to the chamber changes. The focus will be moved along a plane parallel to the directrix plane. To reposition the focus in TCC, wherefore, we need to move along  $z$  and the other vector which defines the directrix plane. This second axis will be called  $x$ . To complete the  $\mathcal{R}^3$  basis, the natural direction of the third axis is the one perpendicular to the directrix plane. This will reposition the focus in TCC in case of a rotation around  $b$ . The pointing of this vector, called  $y$ , will be for convention upwards.

The system of five axes defined  $(x,y,z,a,b)$  allows to correct for astigmatism in TCC. From the six DOF of the Hexapod, one does not need to be employed.

The next step is to define these five DOF in the Hexapod software. To do so, the *Tool SOC* origin has been set in the centre of the OAP reflecting surface with two of the three axes parallel to  $a$  and  $b$ . The *Work SOC* has been positioned with its axes parallel to the set  $(x,y,z)$  with its origin congruent to the one of the *ZERO SOC*.

Now we need a link between the notation defined so far and the one of the Hexapod software. This is shown below:

$$\begin{aligned}\text{Rotation around: } & a = y_{\text{tool}} \Rightarrow \text{U} \\ & b = x_{\text{tool}} \Rightarrow \text{V}\end{aligned}$$

All the rotations are counter clockwise for positive rotations by default.

The new set of SOCs is shown below:

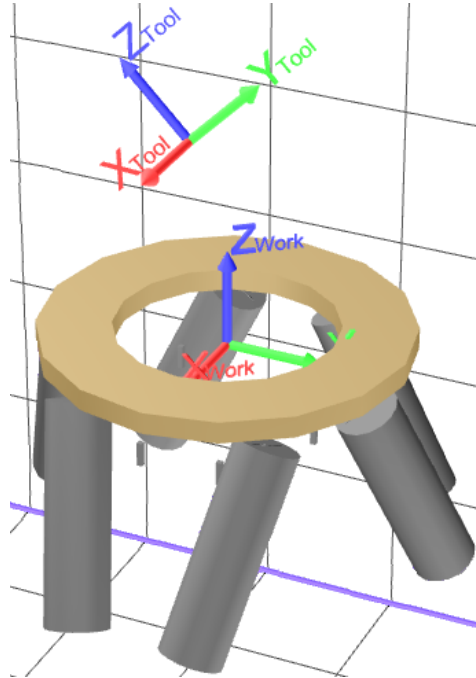


**Figure 4.3:** The new *Work* and *Tool SOC* as they look in the PI software.

### 4.3 Focus adjustment procedure

In this section the focus adjustment procedure will be explained and the improvements necessary to make it faster will be exposed.

In the LION cave the focus analysis is done using two cameras mounted on a microscope whom objective has its focus in TCC (see figure 3.1).

In the case of good OAP alignment, what the user sees in the microscope cameras are the beam sections along  $z$ . If the beam is astigmatic, there will be planes where the beam will look elliptical. As said in the previous section, there are two cases of astigmatism based on the orientation of the ellipse axes:

- 1- Ellipse axes parallel to the camera edges  $\Rightarrow$  Vertical astigmatism
- 2- Ellipse axes rotated by  $45^\circ$  respect to the camera edges  $\Rightarrow$  Oblique astigmatism

The corrections for these cases are listed below:

- To correct for [1]  $\Rightarrow$  Increase/decrease  $U \Rightarrow$  Shift along  $y \Rightarrow$  Shift along  $z$
- To correct for [2]  $\Rightarrow$  Increase/decrease  $V \Rightarrow$  Shift along  $x \Rightarrow$  Shift along  $z$

All the other possible cases of astigmatism are a mixture of both [1] and [2] and can be corrected combining the two procedures.

Once the beam has a circular shape, we need to check the other planes perpendicular to  $z$ . Here, if the beam is not round shaped the same procedure should be applied and the planes previously corrected need to be rechecked.

If these corrections have been successfully applied, the beam should be round shaped both before and after the focal plane. The last step is necessary to overlap the OAP focus to TCC. This has to be defined before starting the beam-time and should be marked in both the cameras.

The overlap of the OAP focus with TCC is not a condition sufficient to state that the beam is well aligned. Another condition is the axis of the laser going through the focus. Some acceleration mechanisms (e.g. RPA) work more efficiently in laser propagation direction. Also diagnostics, as back reflex measurements, can be influenced by this angle. Due to this, only small angular corrections can be imposed by the Hexapod during alignment procedures. If a larger angular correction is required mirrors previous to OAP have to be used.

## 4.4 A program for the alignment routine

What slows down the alignment procedure exposed so far are the two steps done for each correction. The first one for the rotation and the second to bring the beam back in TCC. Furthermore, the lack of a measurement of the focus roundness during the beam-times makes the procedure qualitatively judged by the operator. To merge the two steps in one and have all the necessary focus analysis at the same time, a LabVIEW program has been developed. The merging of the two steps is done coupling the axes of the Hexapod. A translation is automatically applied everytime a rotation is done. The focus analysis is done calculating the necessary quantities out of SIDs.

The program has been tested using the following set-up:

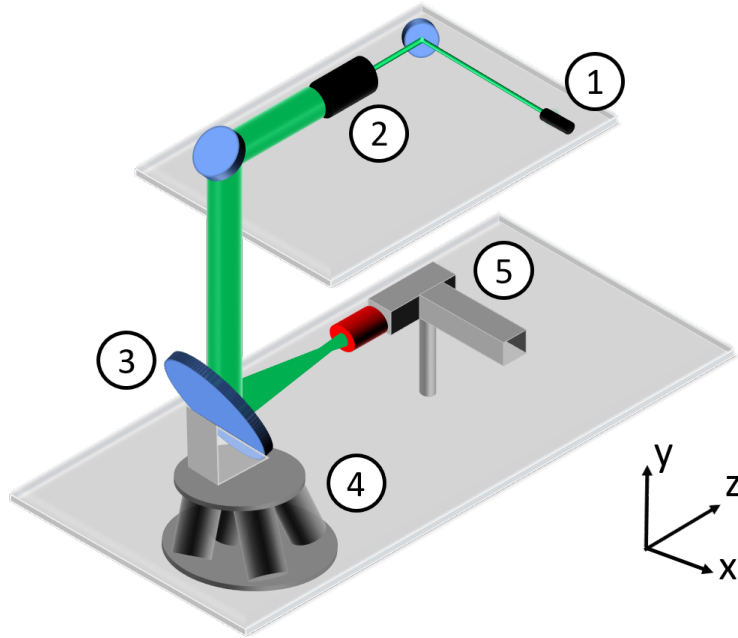


**Figure 4.4:** A laser beam is emitted by a Greeny (1). It is sent through a beam-expander (2) and focused by OAP (3), which is mounted on a Hexapod (4). Finally, a microscope (5) with an objective (in red) images the beam on two cameras.

OAP, the Hexapod and the microscope used are the same of the LION side chamber. OAP has a diameter and a focal length of 20 cm.

The microscope has both the Low and the High Mag mounted on it. The focus pictures shown in this chapter have all been taken with the High Mag.

The model of the Hexapod used is: H-824K016.G2V (details can be found in [29]). This Hexapod has a  $0.5 \mu m$  resolution for translations and  $2 \mu rad$  for rotations. These are way below the minimum increment needed to make a correction visible in the cameras.

The front panel of the program is shown in figure 4.5. The program has two main functions; focus adjustment (on the left) and focus analysis (on the right).

In the front panel, pictures taken by the camera chosen and the position and the velocity of the Hexapod axes are always visible.

The main functions of the program will be explained in the following. For a full guide to the program the reader can refer to the manual in the appendix.

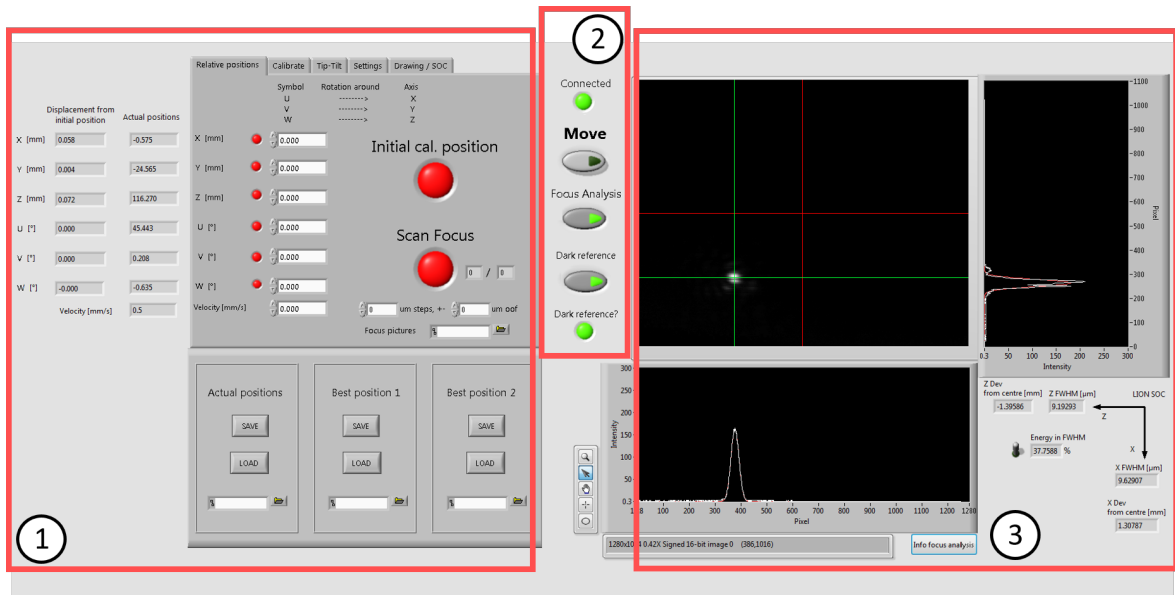
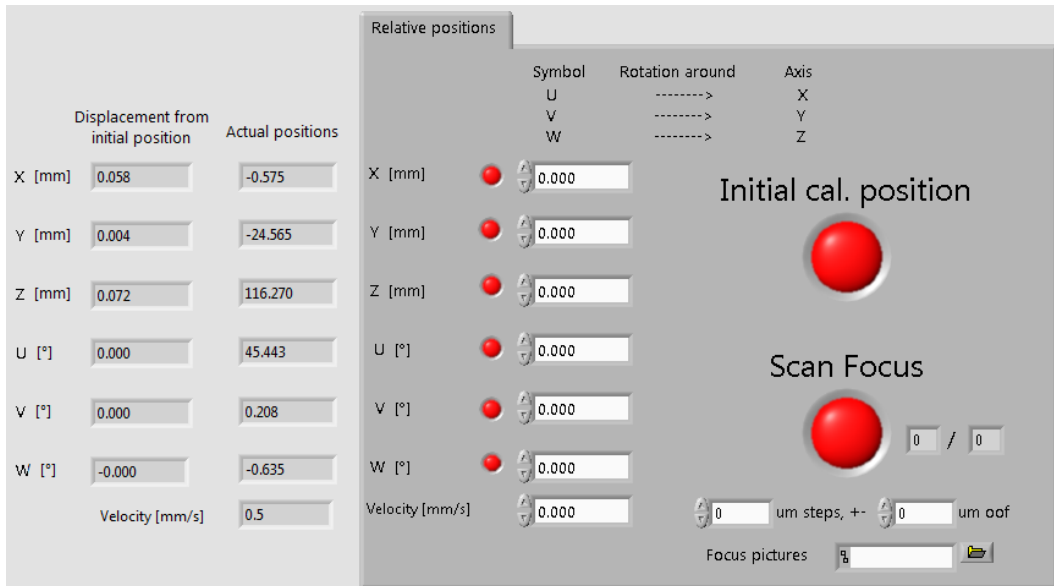


**Figure 4.5:** Front Panel of the LabVIEW program:

1- Hexapod control unit    2- Main control unit    3- Camera control unit

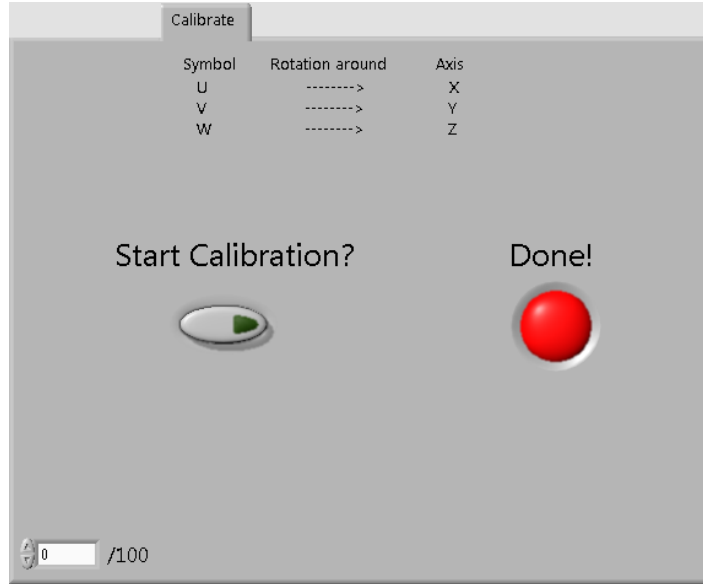
#### 4.4.1 Relative positions



The left part is fixed in the front panel. It shows the positions relative to the starting point (left column) and the positions relative to the *ZERO SOC* (right column). In the section *Relative positions* the user can move the Hexapod along each axis separately and set their velocity. The axes are defined according to the choice given in the previous section. The function *Initial cal. position* is related to the section *Calibrate* and will be

explained later. The button *Scan Focus* can be used to scan the focus in  $z$  dimension and record different pictures for step sizes defined by the user. The importance of this function is crucial to reconstruct the laser wavefront (see 5th chapter).

#### 4.4.2 Calibrate



As mentioned previously, the program is designed to keep the laser spot in TCC position while adjusting it. An angular change of OAP has thus to be compensated by lateral displacement of the beam. To evaluate that coupling a calibration has to be done. The principle of the calibration is measuring the displacement of the beam after applying a certain angular change ( $\Delta U$ ) and in the second step a certain lateral variation ( $\Delta y$ ). Before explaining the calibration procedure, we need to define the quantity  $P(x,y)$ . This is the position in pixels of the beam centre of light. The coordinates  $(x,y)$  are relative to the camera top-left corner.  $P(x,y)$  can be calculated as follows:

$$P(x,y) = \left( \sum I(x,y) \cdot (x,y) \right) / (x,y) \quad (4.1)$$

the sum is done over all the camera pixels. Pushing the *Start Calibration* button, the calibration which couples the axes of the Hexapod begins. The program follows automatically a four steps procedure:

- 1- Move along the  $y$  axis from the initial position,  $y_0$ , to a final position,  $y_1$ .
- 2- Calculate the ratio,  $r_y$ , between  $y_1 - y_0$  and  $P(y_1) - P(y_0)$  (see eq. 4.1).
- 3- Move back to  $y_0$ .
- 4- Apply [1], [2] and [3] to  $U$  and calculate  $r_U$ .

The same procedure is then applied to the couple of coordinates  $(x, V)$ .

$P(x,y)$  has been averaged over twenty pictures for each new position, to avoid the influence of the laser jitter in the calculations.

Finally, we end up with four values and the calibration factors can be calculated:

$$cal_{(y,U)} = \frac{r_y}{r_U} \quad cal_{(x,V)} = \frac{r_x}{r_V}$$

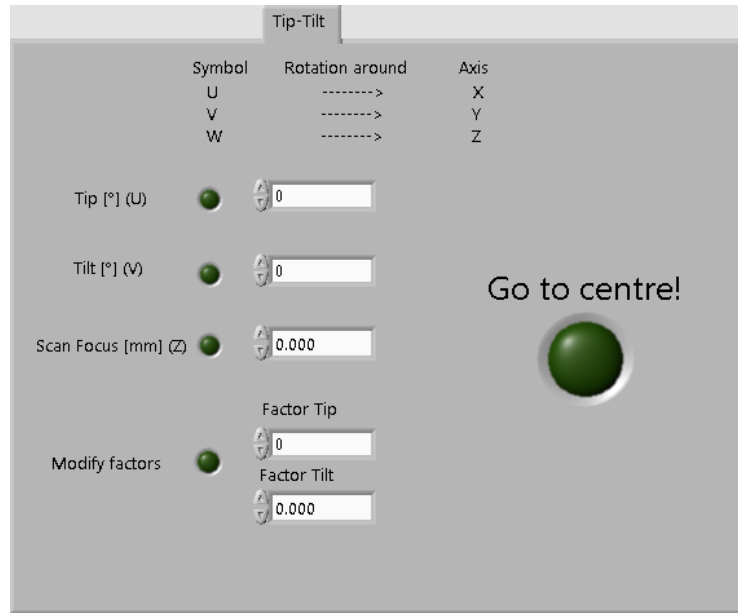
The coupling of the axes is done using these factors. Indeed, when a rotation by  $\Delta U$  is applied, the system translates by a quantity  $\Delta y$  given by:

$$\Delta y = cal_{(y,U)} \cdot \Delta U$$

The same calibration factors can be used, as long as big changes are not done in the set-up. The number of iterations done is displayed in the down-left corner, they are 100 in total. The program takes roughly two minutes to go through all of them. Once the calibration is completed, the button *Done* becomes green and the calibration factors are saved in the section *Tip-Tilt*. The program uses by default the last factors saved, wherefore, if the program is rebooted the calibration does not need to be retaken.

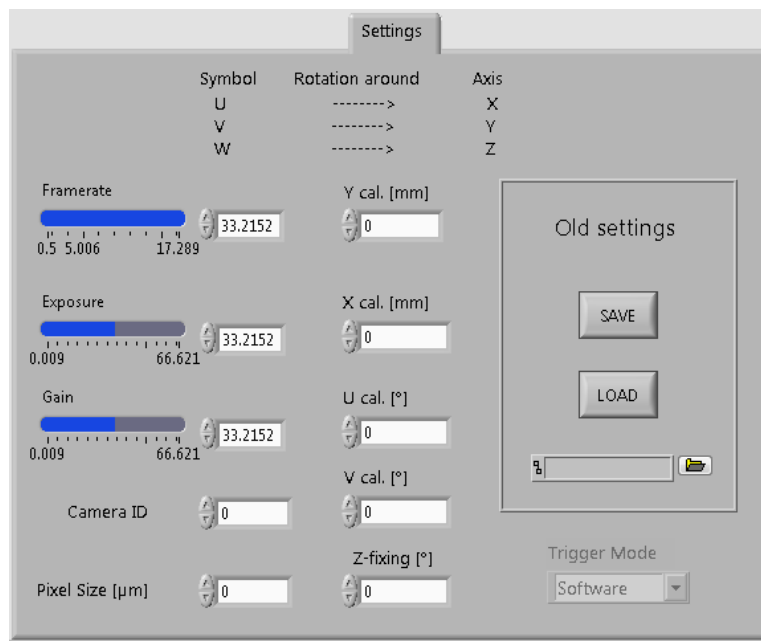
The function *Initial cal. position*, in section 4.4.1, drives the Hexapod to the position where the calibration started. It can be useful if the beam is lost during the calibration.

### 4.4.3 Tip-Tilt



In this section the axes are moved based on the calibration factors. They are now coupled, wherefore, translations along  $x$  and  $y$  are not needed anymore. This is the reason why the only allowed movements are around  $U$ ,  $V$  and along  $z$ . The button *Go to centre!* applies a shift along the  $(x,y)$  plane to set  $P(x,y)$  in the camera centre. In case the calibration factors were not exact, they could be changed in *Modify factors*.

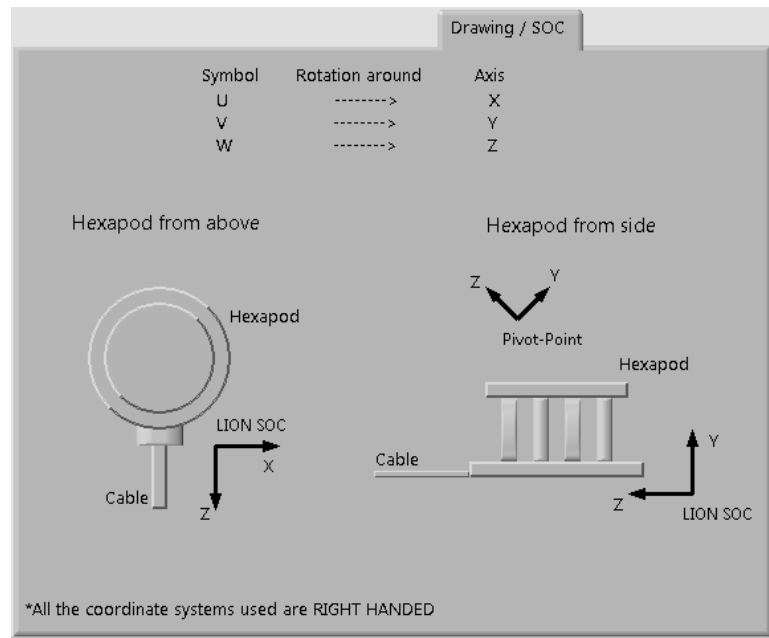
#### 4.4.4 Settings



Here, it is possible to choose the parameters of the camera (trigger, camera ID, etc.) and of the calibration. The last ones have to be chosen in such a way that the beam is fully in the camera field of view after the shifts set. The *Old settings* quadrant allows to save/load all the necessary parameters to start using the program.

In the set-up shown in figure 4.4 and in the LION chamber, the microscope cannot be moved along the  $z$  axis. Therefore, the Hexapod should be moved to scan the focus. This results in a shift of the beam along  $y$ . A “false angle” has been introduced to help the user to fix the focus also along this axis. This correction is called *Z-fixing* $^{\circ}$  and even if expressed in degrees, the program corrects only for translations.

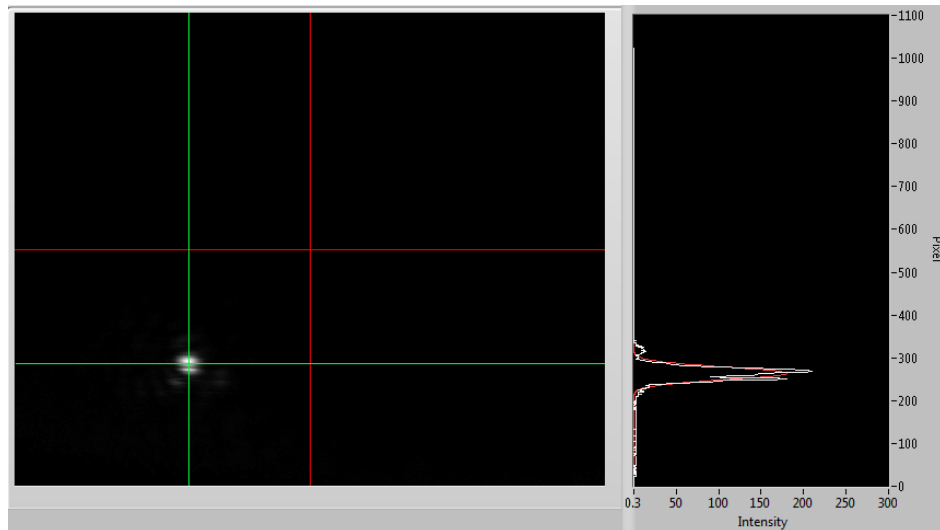
#### 4.4.5 Drawing/SOC



These drawings have been done to help the user to visualize the position of SOCs and PP relative to the Hexapod position in the chamber.

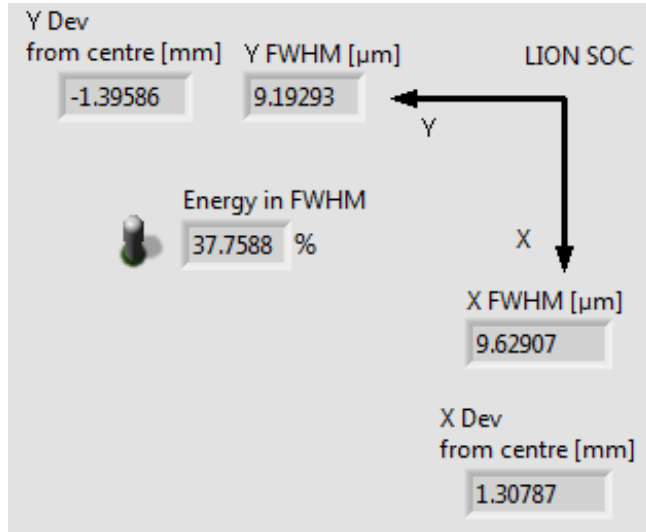
In each section the notation for the axes rotation is reported above.

#### 4.4.6 Focus analysis



Two crosses appear when the *Focus analysis* button is pushed (see figure 4.5). The green cross follows  $P(x,y)$ , while the red one is fixed in the camera centre.

In the picture above a line out is shown for both the vertical and the horizontal line. We expect the beam profile to be Gaussian. For this reason, the normal distribution has been plotted in red for both lines out. The curve has been obtained doing the Gaussian fit of the line out points.



The quadrant above is fixed on the low-right part of the front panel (see figure 4.5) and displays five quantities:

- the two coordinates of  $P(x,y)$  relative to the camera centre
- the two FWHM of the Gaussian fits of the lines out
- the energy enclosed in FWHM of the 2D intensity distribution

The first quantity is crucial to correctly calculate the centring factor to obtain the HDR from the Low Dynamic Range (LDR) pictures.

The second quantity has been just explained before the picture.

The third quantity can be obtained using different procedures. The one used here is based on a geometrical approach. A circle with a diameter of  $FWHM_X + FWHM_Y$  centred in  $P(x,y)$  is cropped. The sum of the pixel intensities in the circle is calculated and divided by the total intensity of the whole picture. If the beam was Gaussian this value would be 50%. A narrower FWHM results in a higher value of the energy enclosed in FWHM. The value displayed by the program is referred to the LDR focus,

this means that the value of the HDR focus is even lower.

Two pictures taken during the focus adjustment are shown below:

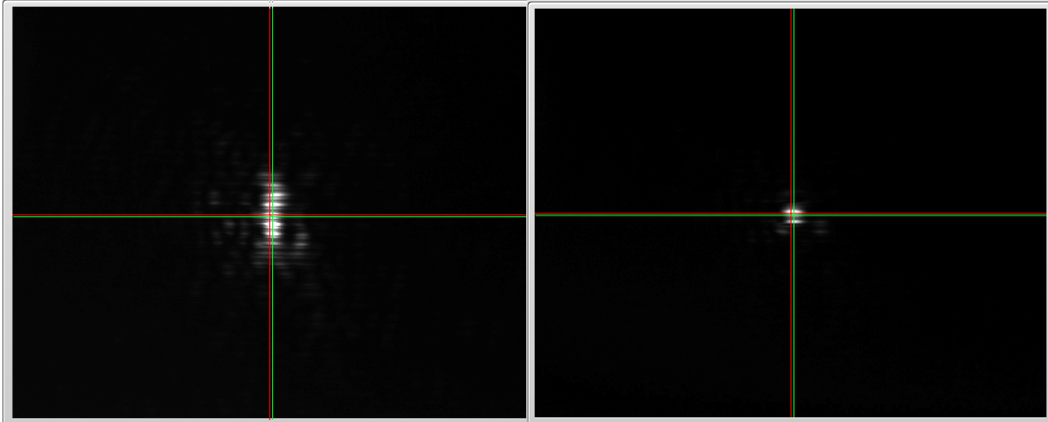


**Figure 4.13:** On the left, the focus before the adjustment procedure. On the right, the focus after the adjustment procedure ( $\Delta V = 0.1^\circ$ ).

In figure 4.13 the stripes are due to the wavelength dependency of the microscope beam-splitter.

Even though a rotation of  $\Delta V = 0.1^\circ$  has been done to correct for astigmatism, the beam stayed in the centre of the camera. Thanks to the calibration, this displacement has not sent the beam out of the camera field of view. Without calibration the beam would have been still visible only if the rotation had been less than  $0.02^\circ$ .

## 4.5 Further improvements

In section 4.3 it has been shown how each rotation results in a displacement along two directions. The program is able to correct only for one of them. It is not able to automatically shift along  $z$ . The correction should be based on the absolute peak intensity and on the FWHM values. The program would need a beam shape recognition. This could become a first step towards a fully automatic focus adjustment procedure. Anyway, the easiness of correcting for astigmatism with the LabVIEW interface already developed would make an auto-focus program superfluous.

An improvement which can still be done is to use the HDR instead of the LDR pictures. One solution could be to mount a higher DR camera rather than the one used so far (see 3rd chapter). Another possibility is to implement a motorised stage with filters in it. The ATLAS-3000 laser, being polarised, could be reduced in intensity just rotating a polariser. HDR pictures could be then reconstructed combining a rotating motorised stage with the pictures taken by the camera.

A factor which slows down the new focus alignment procedure is the necessity of scanning along the  $z$  axis. This limit can be overcome using a Fabry-Perot interferometer, shown in figure 4.14. The user would not need to take pictures out of focus. Thereby, the user would be able to correct for astigmatism without changing the focus or camera position. The higher number of planes displayed in the camera chip would reduce the pixels per plane and, wherefore, make the focus analysis coarser. To solve this problem two cameras can be used, one for the Fabry-Perot and another for the focus analysis. Another issue which can lead to ambiguity during the experiments, only mentioned before, is the following: the chase of best focus could bump in the problem of having a circular shape in the camera even when the beam is still affected by astigmatism.

The reasons for this are the following:

- 1- beam wrongly projected in the camera. Looking at a beam with an elliptical section, there is always a projection which makes it look circular. This effect could be due to the beam or to the microscope misalignment.
- 2- objective focused on one of the two planes in which the astigmatic beam has a circular waist. It can be demonstrated that an astigmatic Gaussian beam has always two planes in which the axes of the ellipse have the same length [30].

In both cases a scan along  $z$  is precise but not fast enough to get an idea about the astigmatism or the alignment of the beam. An immediate way to test if there is a misalignment is to resort to the wavefront and will be explained in the next chapter.

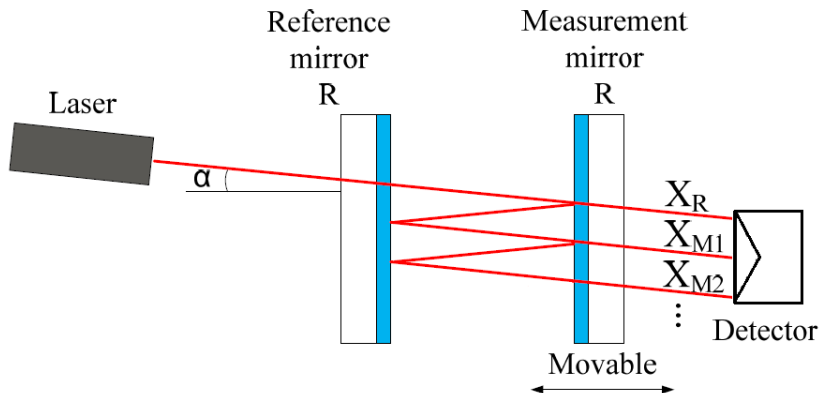


**Figure 4.14:** Principle of operation of a Fabry-Perot interferometer. The beam (in red) is trapped between two highly reflecting surfaces. When the beam impinges on the measurement mirror, a small percentage of it is transmitted and captured by the detector. Here, the multiple reflections generate multiple images ( $X_R$ ,  $X_{M1}$ ...) whom temporal delay between each other can be changed moving the measurement mirror. Picture edited from [31].

# 5 Wavefront retrieval from intensity distributions

In the 3rd and 4th chapter the focus SID has been examined. From a single SID measurement it is not possible to get the phase of the electric field, as the intensity is proportional to the electric field squared ( $I \propto \vec{E} \cdot \vec{E}^*$ ). This limits our knowledge of the spatial laser evolution along  $z$  only to the plane of our measurement. This limitation can be overcome, by taking several SIDs at different positions along  $z$ . Combining these measurements leads to the wavefront and SID along the laser propagation direction. From these two information the beam aberration can be then characterized.

The method to retrieve the wavefront and its implementation in ATLAS-3000 will be the topic of this chapter.

## 5.1 How to obtain a flat wavefront in focus

As explained in the 2nd chapter, the flatness of the focus wavefront is crucial for the ion-acceleration mechanisms. This condition is not enough to reach the highest energy possible in FWHM. For an effective energy transport and beam focusability, it is also desired to have a flat wavefront along the transport beamline<sup>1</sup>. Even small deviations from a flat wavefront can result in a big energy loss, as parts of the beam can be deflected out of the transport mirrors, or focused to positions out of the peak intensity. In both ATLAS-300 and 3000, an adaptive optics (AO) loop is used to evaluate whether the wavefront sent in the beamline is flat or not. In high power lasers, it is required to have a flat wavefront on the compressor, as distortions can lead to damage on its gratings. Therefore, one or more AO loops are positioned before the compressor.

An AO loop is usually made of an adaptive mirror (AM) and a wavefront sensor (see section 5.2). The first is a mirror whose reflecting surface can be shaped by actuators positioned at the rear side of the mirror. The wavefront sensor measures the wavefront and gives a feedback signal to AM, which knows how to warp to correct for aberrations,

---

<sup>1</sup>the path between the compressor and the cave

closing the loop. This stops when the difference between the actual wavefront and the ideal one is below a threshold defined by the user.

During the operation of ATLAS-300, the assumption of negligible effects of the beamline on the wavefront was made, that means it stays flat during its transport. As the ATLAS-3000 beamline is significantly longer, this will induce larger aberration and the assumption can not hold anymore. Therefore, it is planned to correct the wavefront in the focus using a second AO. In particular, the desired AM position is as close to the focusing optics as possible. As the main goal is a flat wavefront in the focus, the AO's wavefront sensor will be included in the microscope.

In conclusion, there will be two adaptive mirrors in the laser chain of ATLAS-3000; one before the compressor and a second in the final part of the beamline.

There is a substantial difference between the two AO loops. In the stretched pulse (on the first AO), the beam has a diameter of 10 cm, wherefore, the reconstruction of the wavefront is quite simple. In the second AO loop, the wavefront is measured in focus, with a beam diameter of the size of a few microns, whereas, on AM the beam has a diameter of roughly 30 cm. This makes the wavefront more difficult to retrieve.

Two solutions to this problem will be presented in the next section.

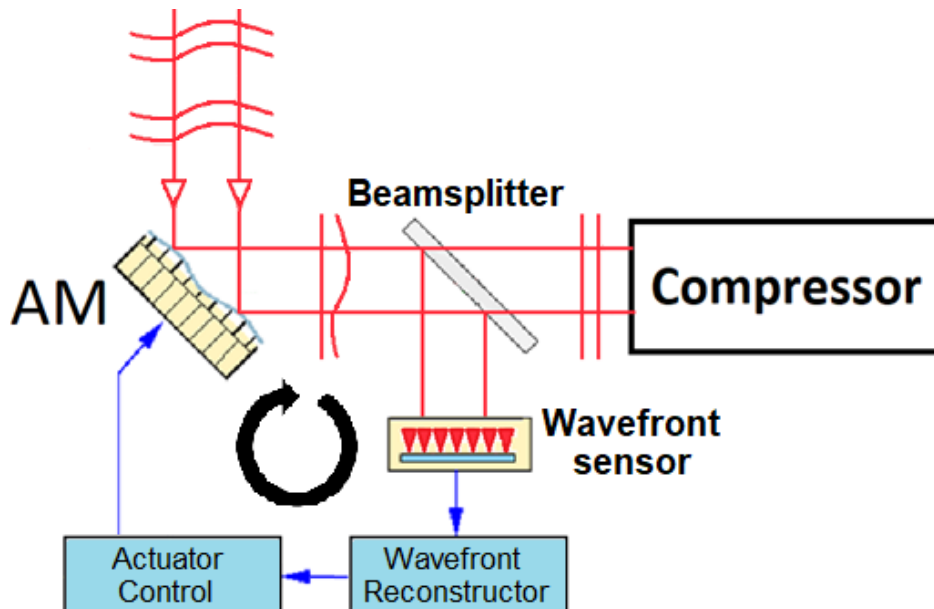


**Figure 5.1:** The figure shows the AO loop positioned before the compressor. The scheme shows a simplified set-up of the one used in ATLAS-300 and 3000. The incoming beam is the one after all the amplifications stages. Picture edited from [32].

## 5.2 Wavefront retrieval methods

To obtain the wavefront, different procedures can be followed. A way to directly display it is a wavefront sensor. These can be of two types; interferometric and non-interferometric. In the interferometric approach, the beam is split in two portions, which are then overlapped. The non-interferometric approach overlaps different portions of a single beam [19].

Because the wavefront sensor will be mounted on the microscope, we choose to use a compact solution. Due to their easy implementation and compactness in the set-up, two wavefront reconstruction methods have been chosen.

The first is a Shack-Hartmann wavefront sensor. This is a non-interferometric sensor, which can be assembled by just positioning a camera in the focal plane of a micro-lenses array. The camera image shows the foci of each lens. Based on their displacement from the ideal position, the wavefront of the beam can be retrieved. The strength of this procedure is the immediacy of the results, which makes it a valid tool for an on-line analysis. The weakness of this approach is the finite lens size, which limits the precision of the reconstruction.

The sensor implemented in the LION cave consists of a microlens array, where each lens has a diameter of  $300 \mu m$ . It can be calculated that a maximum of 900 foci can be displayed in the camera [33].

The second method implemented in the microscope is based on reconstructing the wavefront from intensity distributions in focus and close to it. This is a non-interferometric method, which does not need any extra set-up than the one already built into the microscope.

As said in the introduction of this chapter, one single intensity distribution does not contain information about the phase of the electric field. This can be instead retrieved using more than one picture, taken at different planes. Already with only two pictures, a uniqueness of solutions can be obtained. Indeed, there is only one possible wavefront, which links one SID with a second obtained propagating the first a distance  $z$ .

The main idea behind this wavefront retrieval method is the Gerberth-Saxton algorithm [34]. The two SIDs used in this case are the ones of the near and far field. The algorithm retrieves the wavefront based on the known relation between this two planes (see 2nd chapter).

What we want to understand now is if this algorithm could fit our case. Focusing the

beam with a  $90^\circ$  OAP, the far field can be seen at the OAP focal plane and the near field just after OAP. In the LION set-up, the microscope can display SID in focus and close to it. This means that the near field SID is missing and the Gerchberg-Saxton algorithm cannot be applied. As second SID, we are forced to use a plane close to the focus. As a direct consequence, the Fourier transform is not linking the two SIDs and another propagator needs to be defined. Thanks to diffraction theory, a propagator gives  $\vec{E}$  in any plane, starting from a known  $\vec{E}$  in one plane parallel to the first.

The general idea behind a wavefront retrieval algorithm, based on propagation, is shown in figure 5.2. Here  $A$  and  $B$  are the  $\vec{E}$  amplitudes in the two planes compared. In particular,  $A$  and  $B$  are the ones of the known SIDs, instead,  $A'$  and  $B'$  the amplitudes retrieved.  $\phi$  and  $\theta$  are the phases of the two  $\vec{E}$  and their subscripts represent the number of iterations already done ( $n$ ). Figure 5.3 shows the mechanism which makes the algorithm working. The radii of the circles,  $a$  and  $b$ , represent the  $\vec{E}$  amplitudes of the known SIDs at two random points in the first and second plane respectively.

An alternative way to approach this problem is explained in [35]. Here, it is shown how instead of a second SID, more constraints can be imposed to the system to have a fast converge of results.

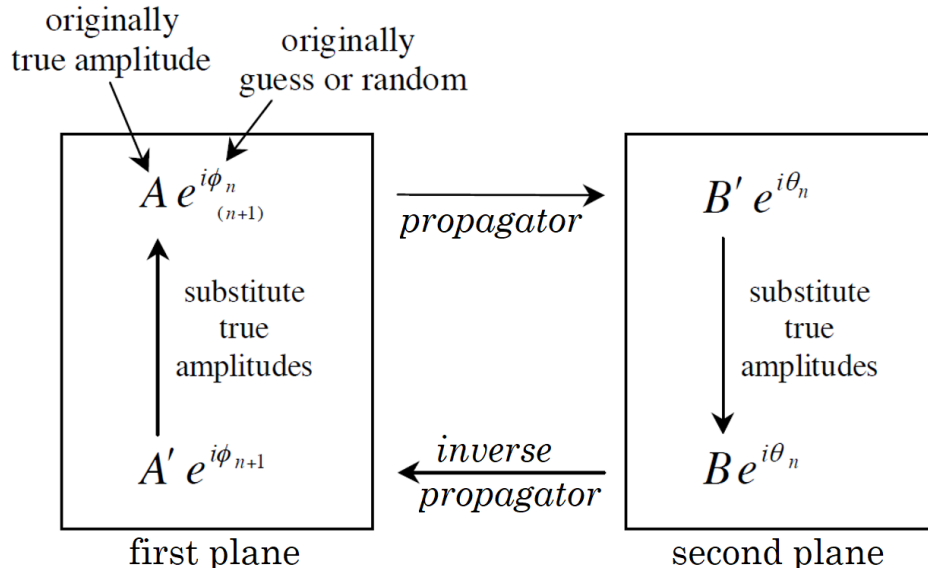


**Figure 5.2:** In this picture is shown a wavefront retrieval algorithm. It corresponds to the Gerchberg-Saxton algorithm, when FT is used as propagator. In this particular case, it is possible to retrieve the wavefront by substituting the intensity in two transverse planes related by FT. In general, the algorithm is valid when two SIDs are related by a spatial evolution defined by the diffraction theory. Picture edited from [36].

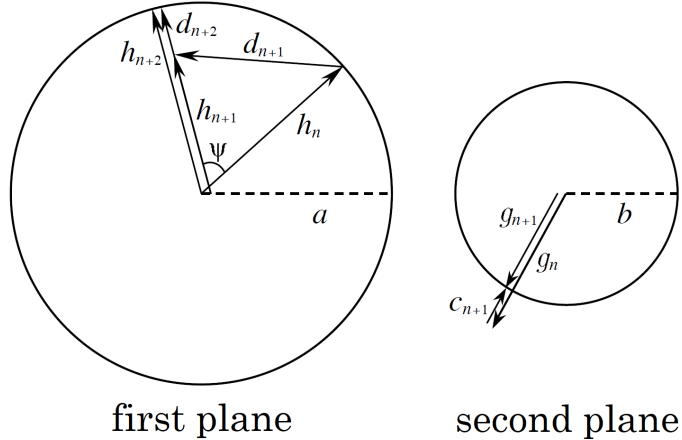


**Figure 5.3:** The working principle of the wavefront retrieval algorithm is shown. A variation in intensity in the second plane results in a change of phase by  $\psi$  in the first plane, when the inverse propagator is applied ( $g_{n+1} \Rightarrow h_{n+1}$ ). One of the two planes is taken as reference, in the picture the second. Picture taken from [36].

The next goal is to apply this algorithm to the laser focus of the LION chamber. A Matlab script has been written using LightPipes as set of functions, to succeed on this purpose.

### 5.3 The role of the propagators in the wavefront retrieval algorithm program

To make the wavefront retrieval algorithm running, three quantities are needed:

- 1- a seed to start the loop
- 2- two SIDs in two parallel planes along  $z$
- 3- a propagator

The seed of the loop will be a flat distribution both in phase and intensity.

The two SIDs will be two pictures, taken in and  $50 \mu m$  out of focus (towards OAP). These have been taken during the LEX beam-time of the 26/10/2016.

Before choosing the propagator, the right precision and approximation of the system has to be defined. In the LION set-up in ATLAS-3000, two OAP can be chosen, one has a numerical aperture of  $f/1$  and another of  $f/2$ . In ATLAS-300, instead, only a

$f/2$  OAP was used. As shown in [37], the Fresnel gives already a good approximation of both set-ups. The Fraunhofer approximation would results too coarse, indeed, its validity is limited only within  $z_r$ .

Besides the quality of focus approximation, the run time of the algorithm is also a criterion for the final propagator decision.

LightPipes for Matlab allows to define four propagators:

- 1- **LPForward**: the analytical solution. It directly solves the integral 2.4.
- 2- **LPSteps**: it takes into account for different materials of the medium the beam propagates through.
- 3- **LPForward**: it is based on the Fresnel approximation. It solves the expression 2.6.
- 4- **LPFresnel**: it directly solves the integral of equation 2.5.

The LPForward propagator is too slow and leads to an unneeded high precision.

The LPSteps propagator does not fit our needs, as the beam purely propagates in vacuum.

Thus the matter of choice in our case is either the LPForward or the LPFresnel propagator.

For setting up and optimizing the retrieval loop, we set up a test case, using a Gaussian beam.

The idea behind this test is to compare the theoretical wavefront with the one obtained propagating from  $z=0$  to a plane where  $z$  has a value of few tens of the Rayleigh length, using one of the propagators LPForward or LPFresnel.

The theoretical results have been calculated using the Matlab script in the appendix. The wavefront in the plane out of focus, after the LightPipes propagation, has been printed out using the function LPPhase.

Before proceeding a clarification has to be done: when we talk about the wavefront in one plane, we refer to the total phase the photons have with respect to the first photon reaching the plane. Total means that the phase is calculated without subtracting multiples of  $2\pi$ .

The comparison between the different methods will be done comparing the spatial derivative of the wavefront. The reason behind this is the following: a shift in phase does not result in an aberration but just in a piston, which does not change the shape

of the wavefront. Furthermore, the parabolic shape of the ideal case makes the comparison difficult to be seen. The spatial derivative can be also used to preserve the character of each distortion but still showing the meaningful differences between the ideal and the reconstructed wavefront. The results are shown below in figure 5.4.

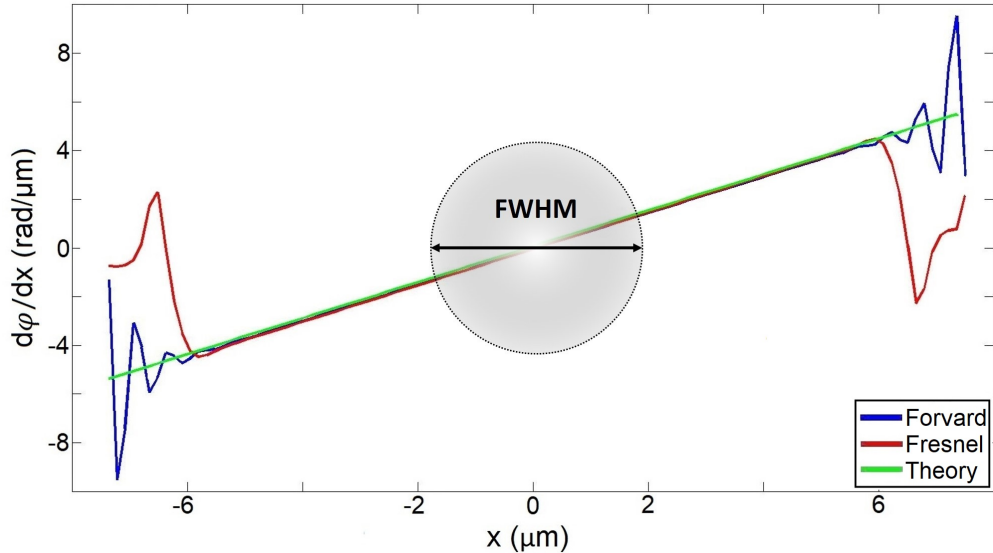


**Figure 5.4:** The spatial derivative of the wavefront is shown for the theoretical (green), LPForward (blue) and LPFresnel method. The grey halo represents the area within FWHM of the beam reconstructed. The wavefront is calculated  $10 \mu m$  out of focus and simulating a Gaussian beam with  $w_0 = \lambda$ . The good agreement of the three curves within FWHM shows how the two LightPipes propagators can be actually used for the wavefront retrieval algorithm.

The results in figure 5.4 show that the LightPipes propagators overlap perfectly in FWHM but, far from it (around  $\pm 6$ ), they behave differently. This will end up in an artefact in the algorithm which will be analysed in the next section.

### 5.3.1 Main dependencies of the algorithm

Once found the well agreement with the theoretical result, the propagators have been used to write the wavefront retrieval algorithm. The program with the algorithm, written in Matlab, can be found in the appendix.

Before showing the outcome of the algorithm, it is necessary to understand how it has been built and why. LightPipes defines a field starting from a grid, whose side is long *size* and with a number of meshes  $N^2$ . The ratio between *size* and  $N$  defines the *pixel size*. Each pixel acts like a single source, according to the Huygens-Fresnel

principle (see 2nd chapter). LightPipes propagates the intensity in the grid based on the wavefront of the field. The grid-nature of the propagation strictly binds the outcome of the algorithm to  $N$  and *size*. The results of this chapter have been obtained using a grid size of  $55 \mu m$  with 500x500 pixels. These values have been chosen such that the resolution of the algorithm is the same of the microscope's cameras. Once the grid has been defined, we need to choose how to propagate it. The two SIDs reconstructed 50  $\mu m$  out of focus using LPForward and LPFresnel have been compared to SID recorded by the microscope and to each other. The results are shown below:

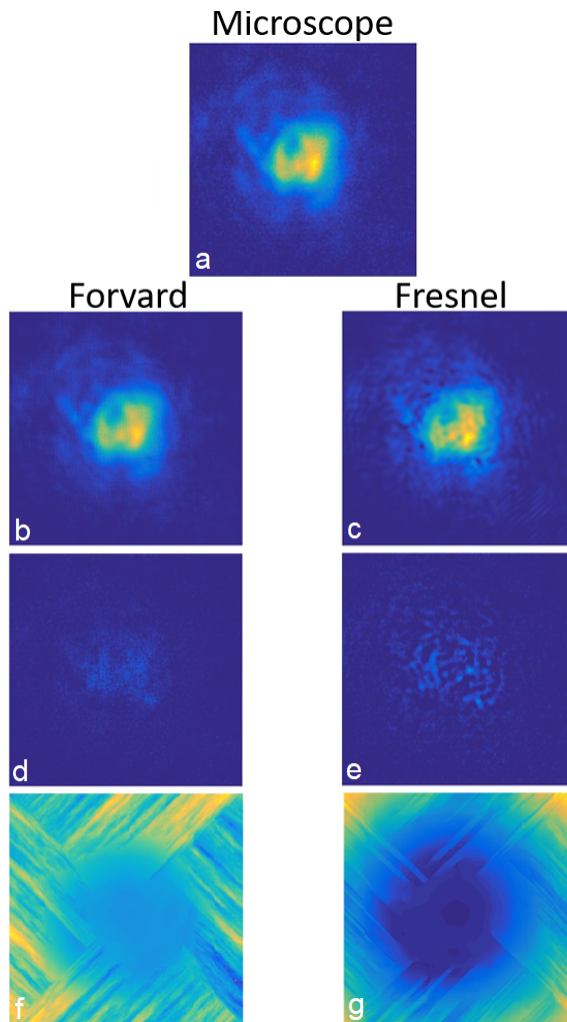


**Figure 5.5:** In (a) SID displayed by the microscope is shown. In (b) and (c) is shown the image reconstructed using in the loop only LPForward and LPFresnel. In (d) and (e) is shown the difference between the microscope SID and the one in (b) and (c). (f) and (g) show the wavefront in (b) and (c).

In figure 5.5 (c) shows a wrinkled pattern, which creates several hot-spots, how can be seen in (e). Furthermore, the time it takes to do 1000 cycles with LPForward is 113 s, whereas, for LPFresnel is 1224 s.

Looking at the two phases, the one in (g) clearly shows the concave shape we expected. The phase in (f) is instead full of cuts, which interrupt the continuity of the wavefront. This artefact, which affects both methods, can be connected to the grid-nature of the LightPipes propagation. This results in deviations from the ideal case as it was already shown in figure 5.4. In conclusion, LPForward has been chosen to compare SIDs, because it results in a faster and more homogeneous outcome. LPFresnel has been chosen to print the phase out from the reconstructed SID, being more precise and less affected by artefacts.

Now that the loop has been built, it is important to understand how to optimise the results. In particular, we are interested in knowing how its accuracy changes with the number of iterations  $n$ . The figure below shows this dependence:

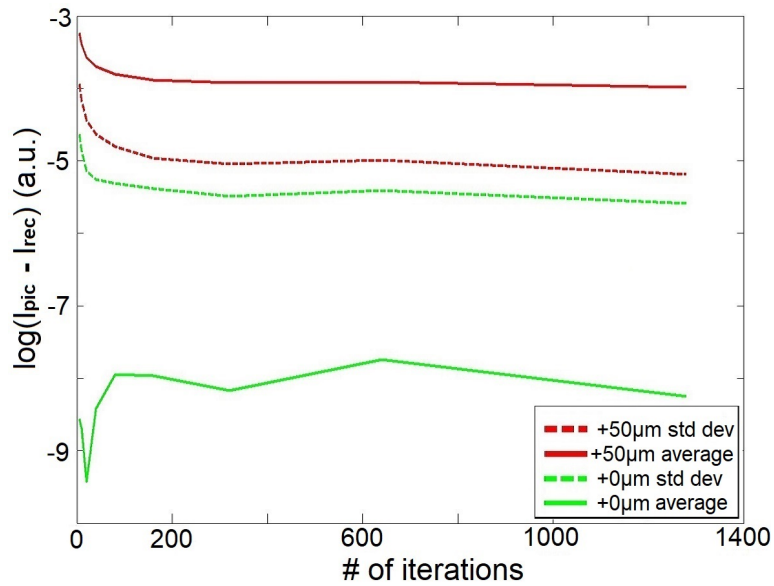


**Figure 5.6:** The plot shows the logarithm of the difference between SID taken by the microscope ( $I_{pic}$ ) and the one reconstructed ( $I_{rec}$ ) as a function of the number of iterations. In the legend, “average” is the total intensity over the number of pixels, “std dev” is the standard deviation of the intensities. They are represented respectively with a continuous and a dashed line.

A similar trend has been also found unveiled in [38].

Figure 5.6 demonstrates how after already 200 cycles there is a good convergence of results but only for  $n > 600$  the  $0 \mu m$  average starts going down.

Even if the results obtained for the  $50 \mu m$  SID brings to larger errors, this will be the one analysed in this chapter. It allows to use a wider area of the camera chip and, wherefore, to have more pixels to compare with the ideal result.

Another interesting dependence is the one given by the number of pictures included in the loop. With the Gerchberg-Saxton algorithm we were limited only to two pictures, but with the loop based on the LightPipes propagators there is no upper limit. Because a narrow focus scan was not taken when ATLAS-300 was on, this dependence cannot be reproduced in our case. The results have been taken from [39] and are shown in figure 5.7.

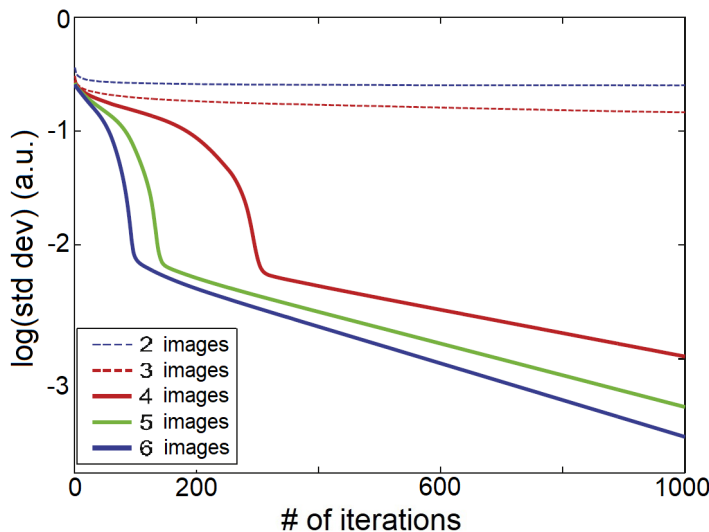


**Figure 5.7:** The plot shows the logarithm of the standard deviation (std. dev.) of  $I_{pic} - I_{rec}$  as a function of the number of pictures in the loop. It is clear how for a number of images higher than four, there is a change in the trend of the std. dev. Picture edited from [39].

To optimise the result a final improvement needs to be done. The focus scan along  $z$  is done moving OAP, wherefore, the position of the beam along  $y$  changes too. Without correcting for this shift, the wavefront would be asymmetric and SID would have the artefacts shown in figure 5.8. This can be also seen as a proof of the high precision and sensitivity of the loop generated. To include this recentering adjustment in the program, the function ‘centering’ has been implemented in the script of the wavefront retrieval (see appendix).

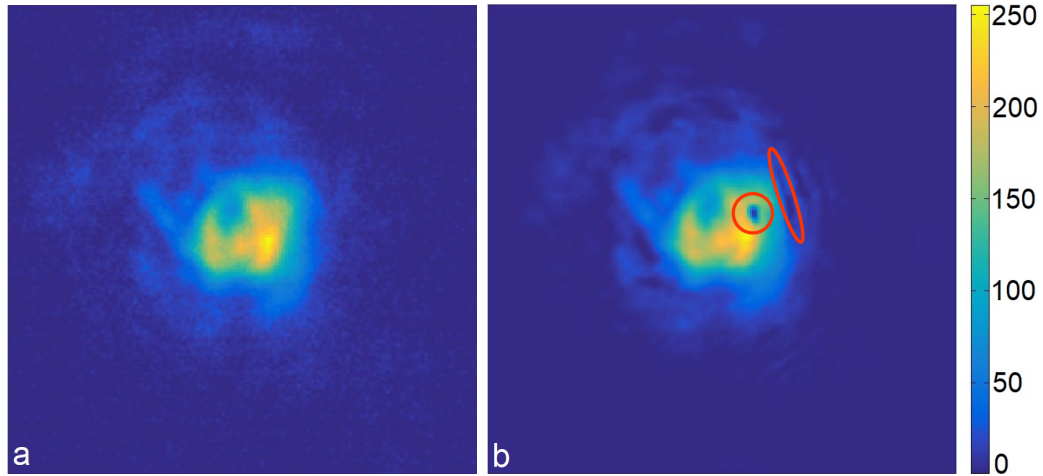


**Figure 5.8:** Artefact due to the wrong alignment of the centre of light. In (a) SID of the microscope is shown, in (b) the one reconstructed by the loop without the function ‘centering’. The regions mainly affected by the misalignment artefact are the ones within the red circles.

## 5.4 Final results and further improvements

Once the main dependencies have been explained, the final outcome of the program can be studied. Thanks to the wavefront and SID retrieved, it is possible to reconstruct the field in each plane and a scan of the focus along  $z$  can be simulated.

The results are the following:

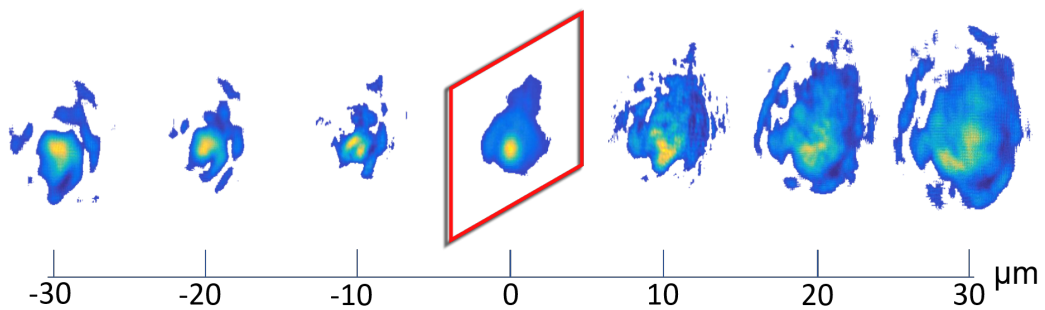


**Figure 5.9:** A scan of the beam SIDs along  $z$  is shown as a function of the distance from the focal plane (in the red square). Each SID in the picture has been normalised to itself but the real values are normalised to the whole distribution. The pictures have been rotated by  $45^\circ$  to give the reader an idea of the beam waist and of the path followed by the beam.

Looking at figure 5.9, it can be stated that the real focus of the beam is somewhere in between  $-10 \mu\text{m}$  and  $0 \mu\text{m}$ . A precise calculation of its position cannot be done

yet because the beam shows a strange asymmetry in SID, probably due to the lack in the loop of a microscope picture along the negative  $z$  axis. Anyway, the wavefront reconstruction is in good agreement with the theoretical results (see figures 5.10). The last has been obtained simulating a Gaussian beam whose waist is given by the OAP diffraction limited focus.

So far only the influence of the wavefront on the spatial distribution has been analysed. Another dependence, which would require a separate chapter, is the one between the wavefront and the temporal distribution, the laser contrast [40].

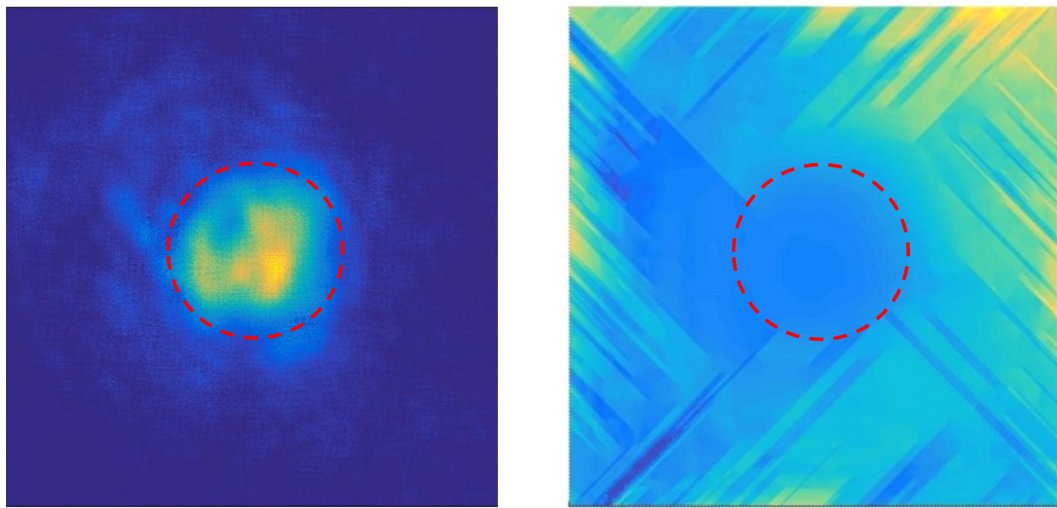


**Figure 5.10:** On the left, the microscope SID is shown. On the right, the retrieved minus the theoretical wavefront is displayed (3D plot in figure 5.12). The two pictures have been compared through the red circle, which is FWHM of the reconstructed SID. It is clear how the cuts do not involve most of the area within the circle.

From the wavefront on the right could be possible to retrieve the different Zernike polynomial contributions. This would make the corrections with the second AM easier to apply.

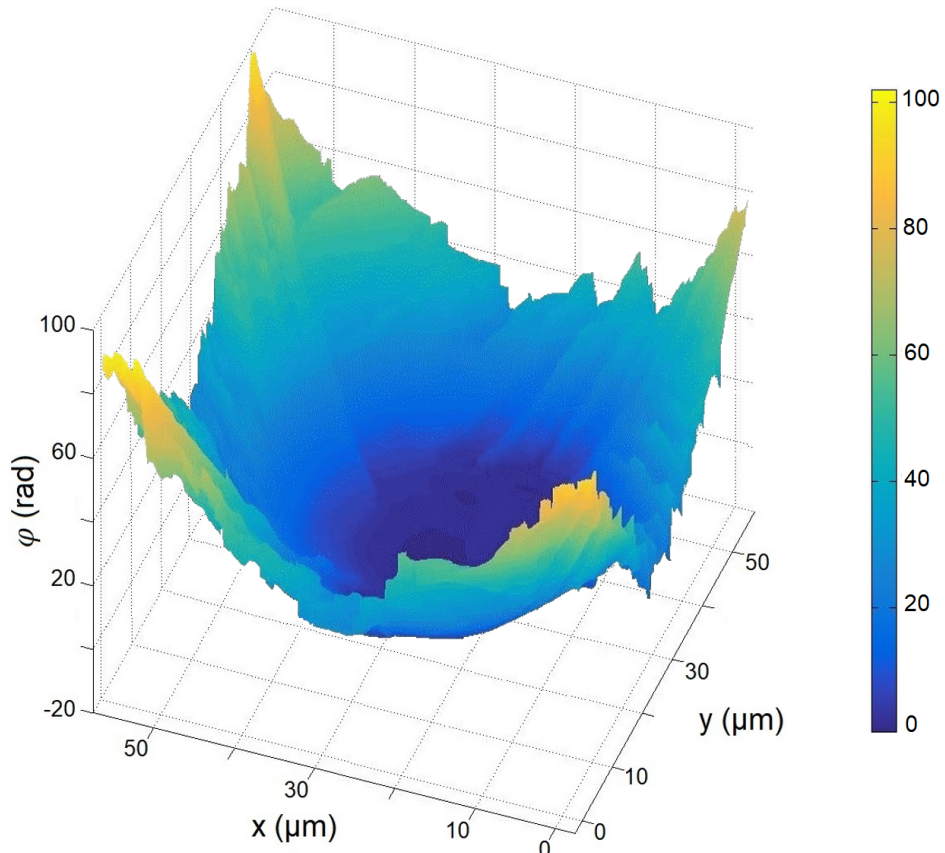


**Figure 5.11:** The 3D plot above shows the wavefront in the plane 50  $\mu\text{m}$  out of focus. Even though its SID looks asymmetric and far from being Gaussian, the wavefront looks symmetric and parabolic. The 3D comparison with the ideal case is shown in figure 5.12.

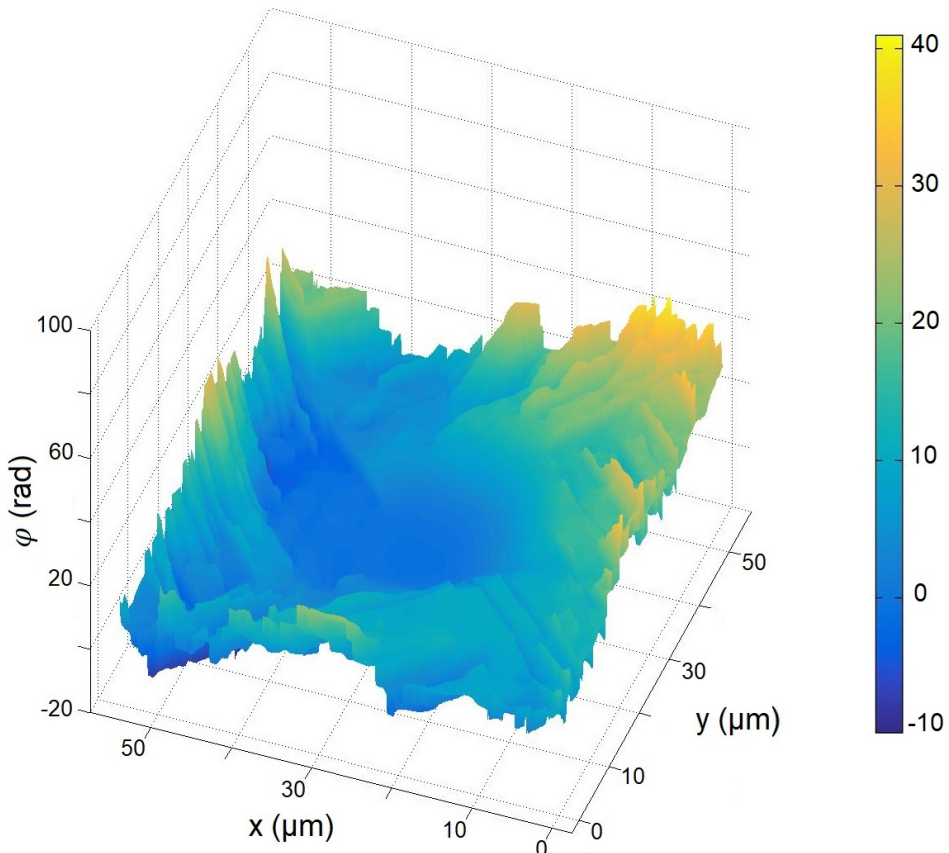


**Figure 5.12:** The 3D plot above shows the difference between the wavefront shown in 5.11 and the theoretical distribution. Basically, what is shown here is the quantity  $a$  in figure 2.3. The 3D plot looks tilted along one of the diagonals. Nevertheless, the wavefront is flatter within FWHM of the retrieved SID, as shown in figure 5.10.

# **6 General conclusions and further developments**

This last chapter wants to be a summary of the results and issues already discussed in the previous chapters, mainly focusing on their future implications.

This thesis has been centred on correcting the focus of a high power laser system from aberration and on its characterisation. The flatness of the wavefront in focus has been set how the ideal goal to achieve. To fulfil this condition experimentally, an AM positioned before OAP will be implemented in ATLAS-3000. The AO loop will be fed by a wavefront reconstruction directly done on the microscope. An algorithm to reconstruct this information out of SIDs has been exposed in the 5th chapter. The implementation of the algorithm in the set-up is the next step which needs to be done to close the loop. This should be based on testing how each portion of AM changes the wavefront and if there is an interconnection between them. The problem will result in a system of multi-variables equations, which one of the solutions is a flat wavefront. Even if the beam was not affected by aberration, it would not be possible to know how the 90° OAP acts on the wavefront. This could be doable only knowing the wavefront before it [41]. What is possible to know, instead, is how the beamline is acting on the wavefront. Indeed, its flatness is assured by the AO loop positioned before the compressor. It would be useful to implement the wavefront retrieval algorithm directly in the LabVIEW program for the adjustment procedure, to have all the focus characteristics available in the same interface. Nevertheless, the main limit of this remains the focus analysis done using only LDR instead of HDR pictures. Some possible solutions to this problem have been already mentioned in the 3rd chapter.

Out of this thesis clearly emerged how a complete characterisation of the laser wavefront could result in a significant improvement of the laser energy on target. In addition, a combined knowledge of wavefront, SID and laser contrast could open the way to a deeper understanding of the ion acceleration dependencies from the laser parameters.



# Appendix

## Ideal wavefront calculation (Matlab script)

The following program has been used to obtain the theoretical values for the wavefront in the different planes. The program simulates a Gaussian beam and propagates it to the desired plane.

```
%Theoretical comparison of the different methods
m=1; nm=1e-9*m; mm=1e-3*m; cm=1e-2*m;
lambda=800*nm;
z=0.055*mm;
size=55*1e-6*m;
N=500;
pixel=size/N;
X=1:N;
Y=1:N;
X=pixel*X;
Y=pixel*Y;
wo=lambda/6;
zr=pi*wo^2/lambda;
k=2*pi/lambda;
R=z*(1+(zr/z)^2);
for i=1:N;
    for j=1:N;
        Phase(i,j)=k*(X(i)-X(N/2))^2/(2*R) +
        +k*(Y(j)-Y(N/2))^2/(2*R);
    end
end
Fr=LPBegin(size,lambda,N);
```

```

Fr=LPGaussHermite(0,0,1,wo,Fr);
I=LPIntensity(1,Fr);
F=LPForward(z,Fr);
Ii=LPIntensity(1,F);
P=LPPhase(F);
P=LPPhaseUnwrap(1,P);
P=P(:,53);
Fi=LPFresnel(z,Fr);
Iii=LPIntensity(1,Fi);
Pi=LPPhase(Fi);
Pi=LPPhaseUnwrap(1,Pi);
Pi=Pi(:,250);
%imshow(P);
%Z=zeros(N,N);
%Z=(sqrt(Phase'))*(sqrt(Phase));
x=[1:1:500];
figure;
surf(x,x,Phase);
%plot(x, P); hold on; plot(x, Phase); hold on; plot(x, Pi);

```

## Centroid function (Matlab script)

The following function takes into account for misalignment during the scan. It recenters the pictures on its center of light. This shift is then transmitted to the wavefront retrieval algorithm which propagates along the right axis.

```

function T=centroid(x,N);
%cx=link;
%N=500;
X=double(imread(x));
X=X(:,:,1);
%imshow(I)
%X=medfilt2(X);
X=mat2gray(X);

```

---

```
rect=[252,203,636,636];
X=imcrop(X, rect);
%[mii , nii]=size(X);
%X=imcrop(X, rect);
G=X;
%H=I2 (:,: ,1 );
%imshow(H)
[ mi , ni]=size(G);
S=max(max(G));
%intensity filter
for ii=1:mi;
    for jj=1:ni ;
        if G(ii , jj)<=S / 2;
            G(ii , jj )=0;
        end
    end
end
G=G/sum(G(:));
[I , J]=ndgrid (1:mi , 1: ni );
I=single(I);
J=single(J);
cent=[dot(J(:) ,G(:)) , dot(I(:) ,G(:))]    ;
recta=[fix(cent(1)-N/2) , fix(cent(2)-N/2) ,499 ,499];
T=imcrop(X, recta );
%figure(1);
%imshow(T)
%figure(2); imshow(X)
%hold on
%plot(cent(1) , cent(2) , 'r.' , 'MarkerSize' ,20);
% figure(2); imshow(X);
end
```

## Wavefront retrieval algorithm (Matlab script)

Below it is reported the Matlab program used to retrieve the wavefront out of two SIDs. The loop compares SIDs through LPForward and prints the phase out through LPFresnel.

```
% LightPipes for Matlab
% Phase reconstruction
m=1; nm=1e-9*m; mm=1e-3*m; cm=1e-2*m;
rad=1;
lambda=780*nm;
size=55*1e-3*mm;
N=500;
z=0.05*mm;
%Read the experimental data of the near and the far field
%intensity patterns from disk:
x=( '\z-sv-pool08\Enrico.Ridente\Desktop\1_nearfield.jpg ');
Inear=centroid(x,N);
%Inear=average(Inear,N);
%Inear=mat2gray(Inear);
y=( '\z-sv-pool08\Enrico.Ridente\Desktop\1_farfield.jpg ');
Ifar=centroid(y,N);
%Ifar=average(Ifar,N);
%Inew=fileout(v,N);
%rect=[1068,574,790,790];
%Inew=imcrop(Inew,rect);
F=LPBegin(size,lambda,N);
FnearOrg=LPSubIntensity(Inear,F);
InearOrg=LPIntensity(1,FnearOrg);
FfarOrg=LPSubIntensity(Ifar,F);
IfarOrg=LPIntensity(1,FfarOrg);

% Wavefront retrieval loop!
for ij=2
    % a=2^(ij-1)
```

---

```
n=1000;
%5*a;
SizeNew=size;%10*mm;
Nnew=N;%250;
%start the iteration:
F=LPBegin( size ,lambda ,N);
for k=1:n;
%progress(k,n,1);
F=LPSubIntensity( Ifar ,F);
F=LPForvard( z ,F);
%F=LPInterpol( size ,N,0 ,0 ,0 ,1 ,F);
F=LPSubIntensity( Inear ,F);
F=LPSubPhase(-LPPhase(F) ,F);
F=LPForvard( z ,F);
%F=LPSubIntensity( Inew ,F);
%F=LPSubPhase(-LPPhase(F) ,F);
%F=LPForvard(-2*z ,F);
F=LPSubPhase(-LPPhase(F) ,F);
end

%Images printed out

FfarRec=F;
IfarRec=LPIntensity( 1 ,FfarRec );
F=LPSubIntensity( Ifar ,F);
FnearRec=LPFresnel(z ,F);
FnearR=LPForvard( z ,F);
InearRec=LPIntensity( 1 ,FnearR );
% for i=1:21
%     tre=(-100+(i-1)*100/10)*10^(-6)
%     Figar=LPForward( tre ,FfarRec );
%     if tre==0;
%         Figar=FfarRec ;
%     end
```

```
% Ifigar=LPIntensity(1, Figar);
% figure(i+20);
% imshow(Ifigar); colormap parula
% Figar=FfarRec;
% end

Fhalfz=LPForvard(z/2,F); Ihalfz=LPIntensity(1,Fhalfz);
Ftwoz=LPForvard(2*z,F); Itwoz=LPIntensity(1,Ftwoz);
Fmhalfz=LPForvard(-z/2,F); Imhalfz=LPIntensity(1,Fmhalfz);
Fmz=LPForvard(-z,F); Imz=LPIntensity(1,Fmz);
Fmtwoz=LPForvard(-2*z,F); Imtwoz=LPIntensity(1,Fmtwoz);
figure(1); subplot(1,3,1); imshow(InearOrg);
figure(56); imshow(InearRec); colormap parula
% subplot(1,3,3); imshow(InearOrg-InearRec); colormap parula;
% print -dmeta '..\figures\man0027_1';
figure(2); subplot(1,3,1); imshow(IfarOrg); colormap parula
subplot(1,3,2); imshow(IfarRec);
subplot(1,3,3); imshow(IfarOrg-IfarRec); colormap parula;
% %print -dmeta '..\figures\man0027_2';
%B(ij)=mean2(IfarOrg-IfarRec)
%C(ij)=std2(IfarOrg-IfarRec)
%D(ij)=mean2(InearOrg-InearRec)
%E(ij)=std2(InearOrg-InearRec)
end

PhiRec=LPPhase(FnearRec);
PhiRec=LPPhaseUnwrap(1,PhiRec);

for ii=1:N;
    for jj=1:N;
        if InearRec(ii,jj)==0;
            PhiRec(ii,jj)=0;
        end
    end
end
```

---

```
figure (3);
%
surf(PhiRec); zlabel('Phase (rad)', 'FontSize', 15);
xlabel('Pixel', 'FontSize', 15);
ylabel('Pixel', 'FontSize', 15); colormap(parula);
shading interp; axis on; view(-70,50);
% %print -dmeta '..\figures\man0027_3';
% %figure (4);;
% %d=1:500;
% %imshow( IfarOrg-IfarRec );
% %Y=Y(250,:);
% %Y=fft(Y);
% %plot(d,Y)
% figure (5);
%
% subplot(1,7,1); imshow(Imtwoz); title(' -100um');
% subplot(1,7,2); imshow(Imz); title(' -50um');
% subplot(1,7,3); imshow(Imhalfz); title(' -25um');
% subplot(1,7,4); imshow(IfarRec); title(' 0um');
% subplot(1,7,5); imshow(Ihalfz); title(' 25um');
% subplot(1,7,6); imshow(InearRec); title(' 50um');
% subplot(1,7,7); imshow(Itwoz); title(' 100um');
% %figure (6);
% %subplot(1,2,1); imshow(Itwoz); title(' 100um');
% %subplot(1,2,2); imshow(Inew);
```

## ***Manual for the focus adjustment procedure***

Program developed in LabVIEW using gar-ex-medsch-09

Name of the program: Hexapod Enrico.vi

Link: Y:\project\lex\AutoFocus

SubVis used: GAIN.vi, FocusAnalysis.vi, NewLive.vi, CalibrationFactors.vi, Difference.vi, new SOC.vi, Tango subVis.

Hexapod used: H-824K016.G2V

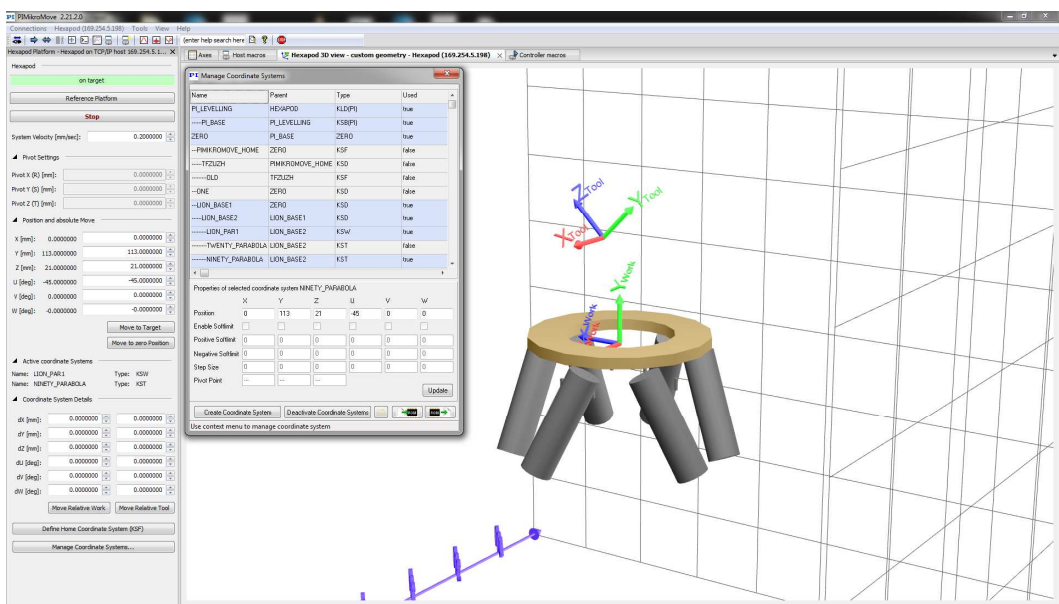
System of coordinates used: LION SOC (fig.1)

Camera used: High Mag. (20x)

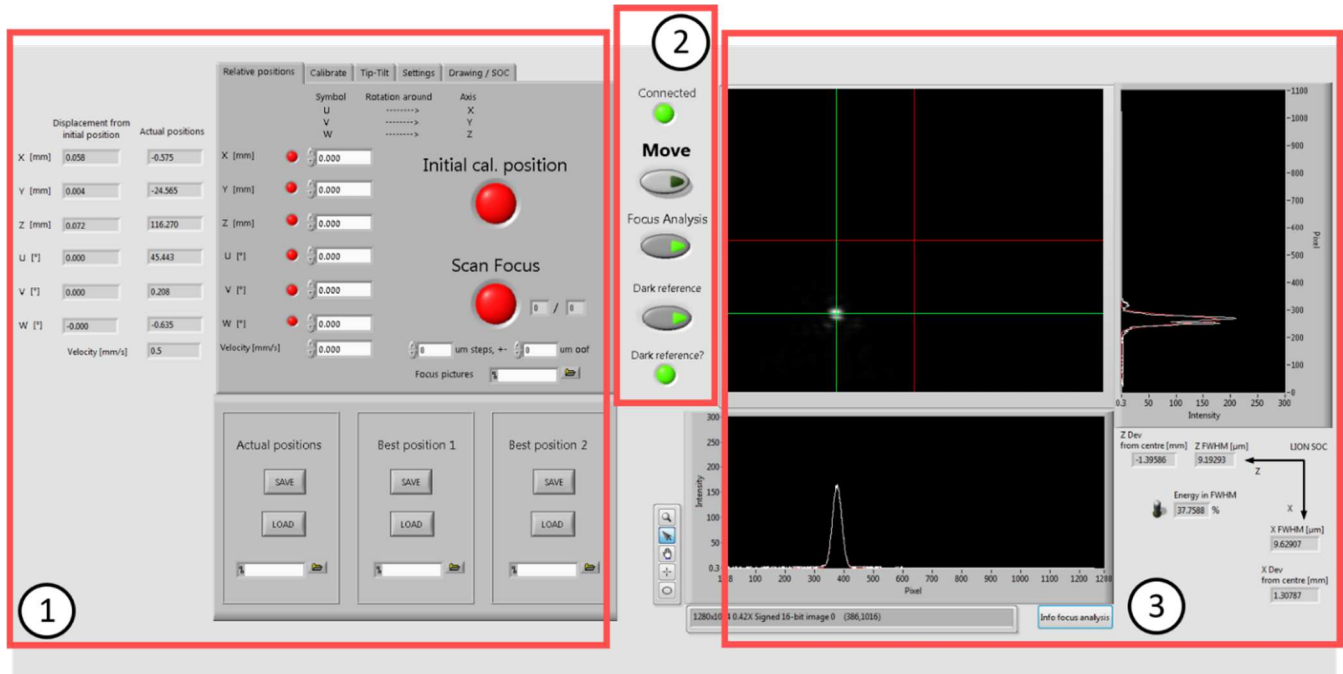
Parabola used: 90° OAP, 20cm focus (parabola used in LEX main chamber)

### **PI SOC: (to apply if a new set-up is used)**

1. Turn on Hexapod control unit
2. Open PIMikroMove and reference axes.
3. Click on *Manage Coordinate Systems* and if a 90° parabola will be used in the experiment, then, all the following SOC have to be activated (blue):  
PI\_LEVELLING, PI\_BASE, ZERO, LION\_BASE1, LION\_BASE2, LION\_PAR1 (Work Coordinate System) and NINETY\_PARABOLA (off-set in mm and deg: 0; 113; 21; -45; 0; 0)  
Instead if a 20° parabola will be used, then, the following SOC have to be activated (blue):  
PI\_LEVELLING, PI\_BASE, ZERO, LION\_BASE1, LION\_BASE2, LION\_PAR1 (Work Coordinate System) and TWENTY\_PARABOLA (off-set in mm and deg: 0; 113; 21; -10; 0; 0)
4. Close PIMikroMove.



## Description of the Front Panel:

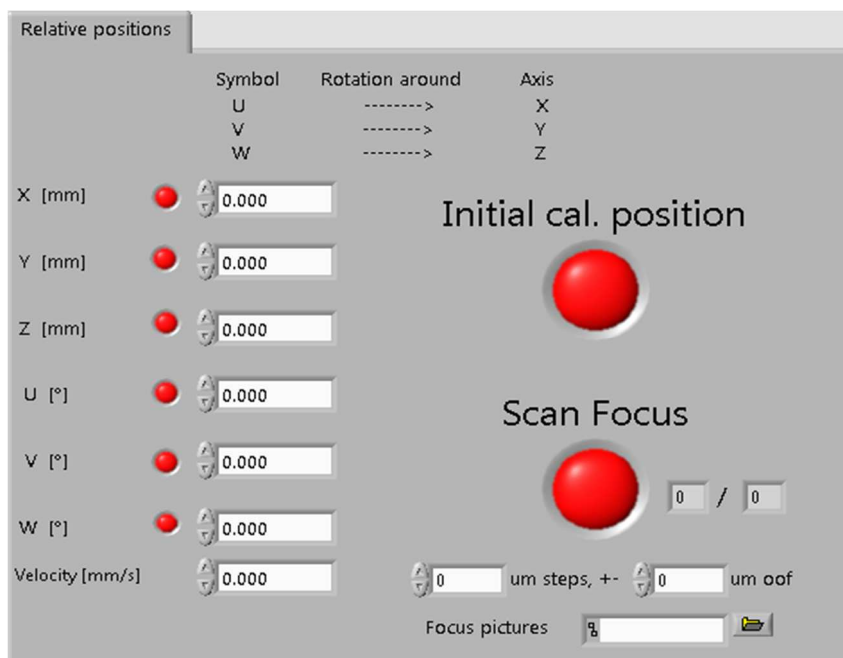


1

1. (From left) The first column, called *Displacement from initial Hexapod position*, shows the difference between the position where the Hexapod is (when the program starts) and the actual position.
2. The second column, called *Actual positions*, shows the distance between the Tool Coordinate System and the Work Coordinate System, the last one coincides with the ZERO SOC (see *PI SOC* section), so if correctly initialized, before moving the Hexapod, the second column should display the off-set of the SOC defined by the user.  
Below the set velocity (max vel. 0.5mm/s).

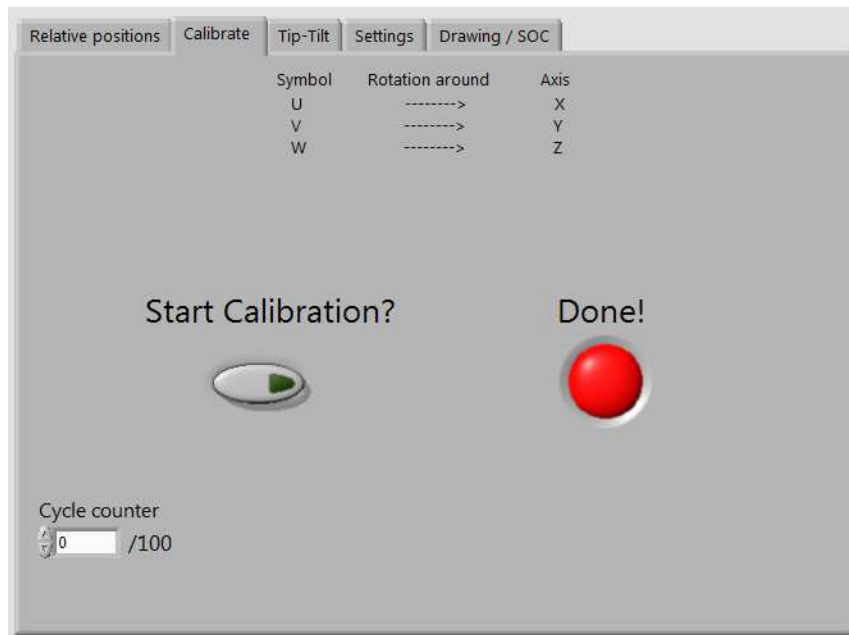
3. Description of the Tab Control:

1. *Relative positions:*



1. The pursuit of the focus can be done using the controls for each axis, which can be activated separately (or not) just pushing the switch beside it. Below the user can set the velocity.
2. *Initial cal. position* drives the Hexapod to the position where you started the calibration (see section *After running the program point 4*).
3. *Scan focus* takes pictures out of focus according to the parameter defined below. It saves the pictures (according to date\_time\_position oof) in the path indicated as *Focus pictures*. (picture below). The counter beside shows how many snapshots have been already taken.

2. *Calibrate:*



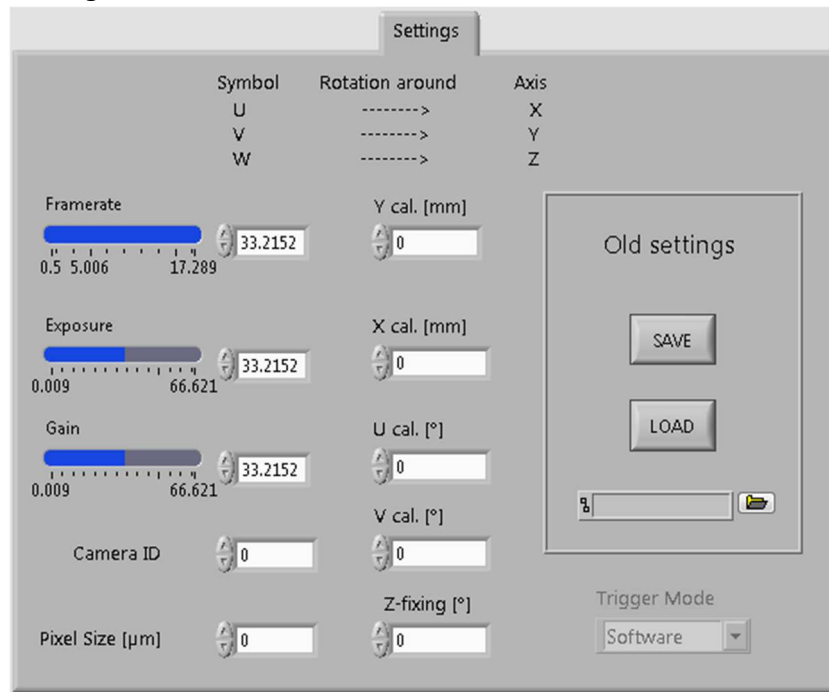
1. Pushing *Start Calibration?* and then *Move* the program starts calibrating the axes of the Hexapod in such a way that, moving Tip-Tilt, the position of the focus in the camera does not change.
2. *Cycle counter* shows how many cycles (over 100) are left before finishing the calibration.
3. *Done* becomes green once the calibration is over.

3. *Tip-Tilt:*



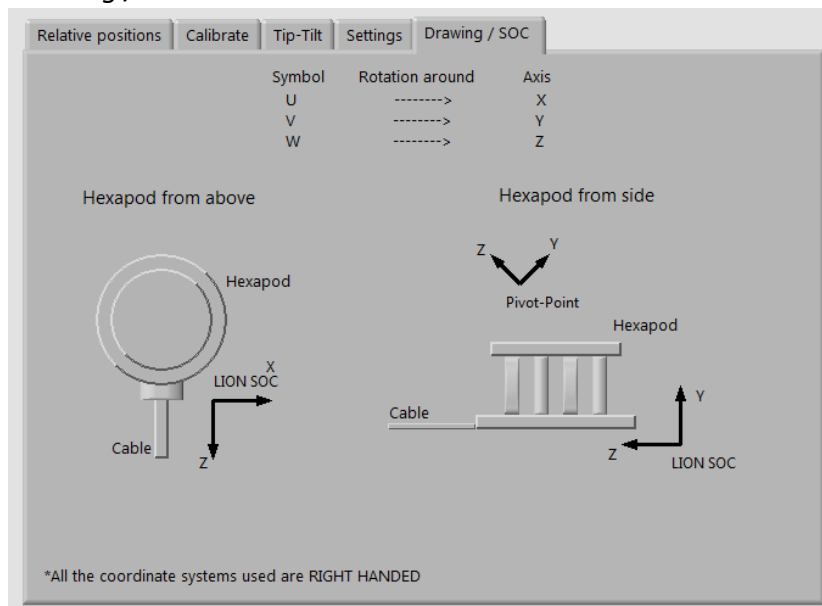
1. To adjust the focus and scan it the first 3 controls can be used, they have to be activated separately (**just one per movement!**).
2. *Modify factors* if activated allows the user to modify the factors out from the calibration, they are fixed as long as the switch is green, otherwise they go back to the values calculated in the calibration.
3. *Go to the centre!* puts automatically the focus in the centre of the camera just translating (without rotating).
- 4.

4. *Settings:*



1. The first column displays the camera parameters (Framerate, Exposure, Gain and Camera ID).
2. The second column displays the parameters for the calibration.
3. *Z-fixing* indicates the angle the user has to correct for to move just along focus direction.
4. *Camera ID*: it is the number of the camera used (check in the uEye software for the ID)
5. *Pixel Size*: can be found in the specifics of the camera. It has to be written in micrometer.
6. *Trigger mode*: It defines in which mode the camera has to work, in free run or trigger mode.
7. *Old settings*: save and loads the last settings in use or previously saved. This are saved in the path below.

5. Drawing / SOC:



These two drawings show the SOC used for LION experiment. The first one is the view from above of the Hexapod (and data cable) and the second one from one side.

The pivot point is showed in the side view and indicates the centre of rotation (defined in PI).

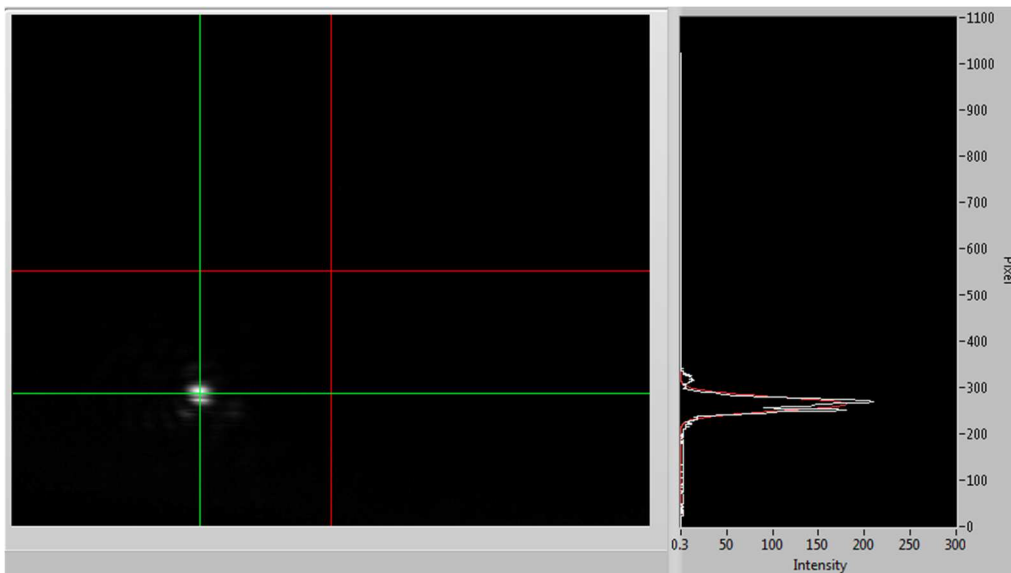
4. The quadrant below allows the user to *Save* and *Load* 3 different positions saved in the path just below each position.



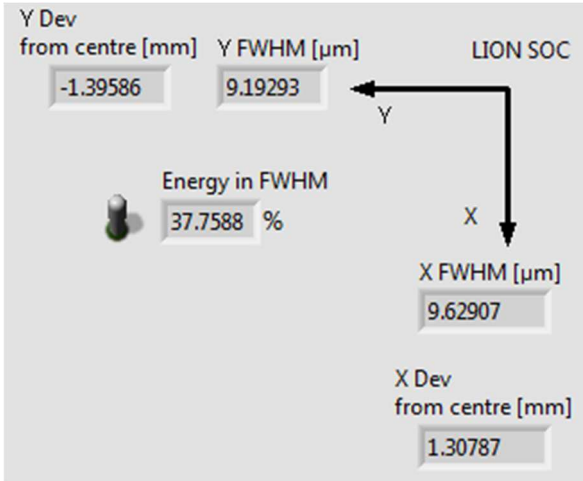
## 2

1. *Connected?* Becomes green if the connection with the Tango server is successful or not. In case it stays red check if the file *start-HekapodPI Enrico.bat* it is correctly opened (see section *Before running the program* point 3).
2. *Move* has to be used every time the user wants to move the Hexapod.
3. *Focus Analysis* displays in the camera two crosses, one red and one green. The red one represents the centre of the camera and the green one represents the centroid (centre of mass/light) of the picture (picture)
4. *Dark reference*: it has to be used when the laser is off. This is necessary for the program to start because it removes the background and the noise from the camera, such that only the focus intensity is taken in account in the calculations.

## 3



1. *Image* shows what the camera sees. The user can zoom (in and out) the picture and right clicking, in the pop-up menu *Palette*, the user can choose the pixel map which fits better the application.
2. On the right the vertical line-out is shown. It is fit with a Gaussian curve (in red), the same is done for the horizontal line-out.

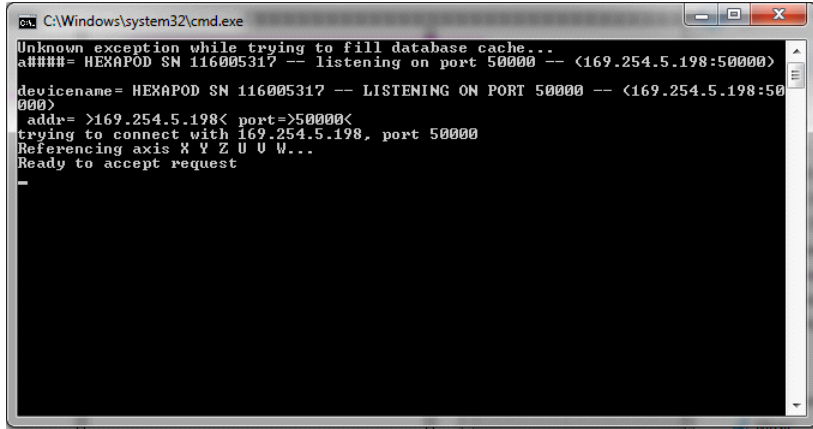


1. *Y (and X) Dev from centre* represent how far is the centroid from the centre of the camera along Z and X respectively.
2. *Y (and X) Std Dev* represent respectively the standard deviation of the green line, in number of pixels, for Z and X respectively.
3. *Energy in FWHM* shows the energy enclosed in a circle with radius the average of FWHM of both green lines. A detail explanation can be found pushing *Info focus analysis*

## Before running the program:

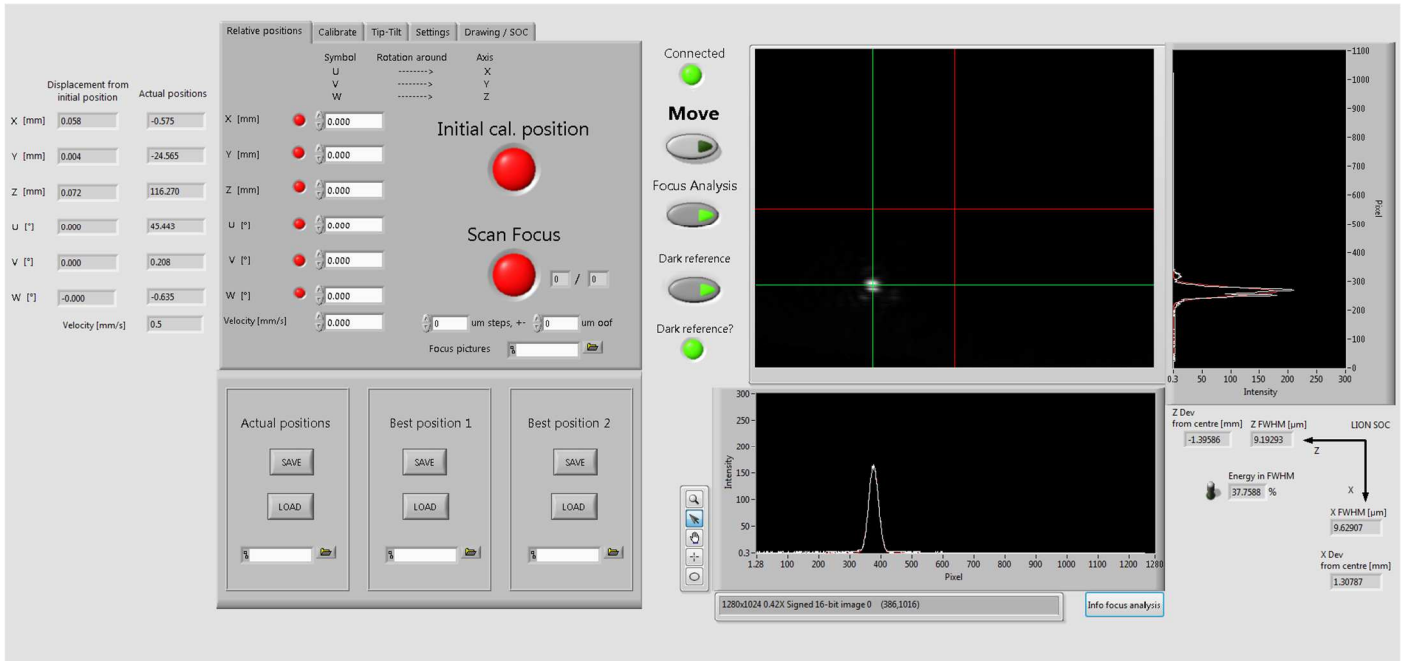
0. If used for the first time with a new set-up see instructions reported in section *PI SOC*.
1. Turn on Hexapod control unit (wait 2 minutes).
2. Turn on and move microscope in focus position.
3. Open the file named *start-HekapodPI Enrico.bat* in the folder: Y:\project\lex\x64 to reference the Hexapod's axes and establish a connection with Tango servers. Once opened wait 2 minutes.

## CHAPTER 6. GENERAL CONCLUSIONS AND FURTHER DEVELOPMENTS



4. Open the program. (picture front panel)
5. Check the Camera ID of the microscope in uEye and write it down in *Camera ID* in section *Settings*
6. (Optional) Load all the paths empty in the program: 3 below the Tab Control (Actual positions, Best position 1 and 2) and 1 in the section *Relative positions* beside *Focus Pictures*.  
The first 3 paths are used to allocate 3 positions of the focus (see section *Description of the Front Panel*) and the last one to save 13 pictures out of focus (see section *Description of the Front Panel*).
7. Run the program

### After running the program:



- 
1. Do the dark reference, therefore turn off the beam
  2. When *Dark reference?* Is green, the beam can be turn on.
  3. Once the beam is entirely visible in the camera, go to focus plane and move the focus to the centre of the camera.
  4. Move along focus direction (big steps, i.e. 1.5mm) and test (using *Focus Analysis*) if the two *Dev from the centre* have changed considerably. If this is the case, go to *Settings* and change *Z-fixing* in such a way that a movement in focus direction does not change the position of the focus in the camera. If this is achieved drive back to focus plane.
  5. Go to *Settings* and check if the calibration parameters are correct. Move the Hexapod by the quantities written and check if the focus is still entirely in the camera or not. If it is not change them in such a way that the beam reaches the hedge of the camera but it is still entirely in it.
  6. Start the calibration (and wait until it is done) to obtain *Factor Tip* and *Factor Tilt*. During the calibration the Hexapod has to move 8 times (10 pictures per movement are taken, except 20 for the initial position). This motions have to be clearly visible in the camera and the beam has to be fully shown.
  7. Go to *Tip-Tilt* to correct the focus and activate **just one axis per movement!**
  8. If the user is not able to find a good focus with this program there is something wrong in the set-up, if this is not the case the problem is in the user itself.
  9. The programmer is always right.

Last update: 13/09/2017

*Enrico Ridente*



# List of Figures

1.1	Relation SID and wavefront . . . . .	3
2.1	Electric field after an aperture; 2D diffraction . . . . .	6
2.2	Off-axis aberration . . . . .	10
2.3	The beam out of a system affected by aberration . . . . .	10
2.4	The Gaussian beam and its main parameters . . . . .	14
2.5	Contrast curve measured with SEQUOIA and TUNDRA . . . . .	19
3.1	Microscope draw . . . . .	22
3.2	Reconstruction of an HDR focus of ATLAS-300 in the side chamber . .	23
3.3	First set-up used to test the HDR camera . . . . .	24
3.4	Second set-up used to test the HDR camera . . . . .	24
3.5	Comparison between pictures recorded with an 8 Bit and the HDR camera and the grey-scale imaged . . . . .	25
3.6	Scheme of the read-out related to pictures taken with different p.d. . .	26
3.7	Comparison between the photodiode and the HDR camera signal . . .	27
3.8	Frame after the slit of the set-up 2 . . . . .	28
3.9	Plots showing the ratios between the peaks of the diffraction pattern .	29
3.10	Frame after the slit of set-up 2 taken with the Greeny in free-run mode	30
3.11	Plot of the ratio between the first order maxima . . . . .	30
3.12	Linear and logarithmic pixel-scheme . . . . .	31
4.1	OAP shape; beam well aligned . . . . .	34
4.2	OAP shape; beam misaligned . . . . .	34
4.3	New SOCs in the PI software . . . . .	38
4.4	Set-up used to develop the LabView program . . . . .	40
4.5	Front panel; overview . . . . .	41
4.6	Front panel; relative positions section . . . . .	41

4.7	Front panel; calibrate section . . . . .	42
4.8	Front panel; Tip-Tilt section . . . . .	43
4.9	Front panel; settings section . . . . .	44
4.10	Front panel; Drawing/SOC section . . . . .	45
4.11	Front panel; focus analysis . . . . .	45
4.12	Front panel; focus parameters . . . . .	46
4.13	Focus fixed after adjustment procedure . . . . .	47
4.14	Fabry-Perot interferometer . . . . .	48
5.1	The AO loop before the compressor . . . . .	50
5.2	The wavefront retrieval algorithm loop . . . . .	52
5.3	Principle of working of the retrieval loop . . . . .	53
5.4	Comparison of the wavefronts obtained with different propagation methods	55
5.5	Comparison between the retrieved intensity and wavefront with Forward and Fresnel in the retrieval loop . . . . .	56
5.6	Loop outcome based on number of iterations . . . . .	57
5.7	Loop outcome based on number of images compared . . . . .	58
5.8	Artifact due to the wrong alignment of the centre of light . . . . .	59
5.9	Scan of the beam reconstructed SIDs along $z$ . . . . .	59
5.10	Comparison between SID and wavefront retrieved . . . . .	60
5.11	3D reconstruction of the wavefront retrieved out of focus . . . . .	61
5.12	Difference between the ideal and the reconstructed wavefront . . . . .	62

# Bibliography

- [1] A. Macchi, M. Borghesi and M. Passoni. Ion acceleration by superintense laser-plasma interaction. *Reviews of Modern Physics*, 85(2):751-793, 2013.
- [2] R.S. Craxton, et al. Direct-drive inertial confinement fusion: A review. *Physics of Plasmas*, 22(11):110501, 2015.
- [3] J.A. Cobble and R.P. Johnson. High resolution laser-driven proton radiography. *Journal of Applied Physics*, 92, 1775, 2002.
- [4] J. Bin, et al. A laser-driven nanosecond proton source for radiobiological studies. *Applied Physics Letters*, 101, 243701, 2012.
- [5] U. Linz, J. Alonso. What will it take for laser driven proton accelerators to be applied to tumor therapy? *Physical review special topics - accelerators and beams*, 10:094801, 2007.
- [6] G.A. Mourou, C.P. Barty, M.D. Perry. Ultrahigh-intensity laser: physics of the extreme on a tabletop. Technical report, Lawrence Livermore National Laboratory, 1997.
- [7] M. C. Newton, Y. Nishinoa, I. K. Robinson. Bonsu: the iterative phase retrieval suite. *Applied Crystallography*, 0021-8898, 2012.
- [8] C. Guo, et al. A review of iterative phase retrieval for measurement and encryption. *Opt Laser Eng*, <http://dx.doi.org/10.1016/j.optlaseng.2016.03.021>, 2016.
- [9] D. R. Luke, J. V. Burke and R. G. Lyon. Optical wavefront reconstruction: theory and numerical methods. *Siam Review*, 44:169-224, 2002.
- [10] G. Baudat. Wavefront analyzer star waves. Technical report, Innovation Foresight, 2015.

## Bibliography

---

- [11] H. Daido, M. Nishiuchi and A. Pirozhkov. Review of laser-driven ion sources and their applications. *Reports on progress in Physics*, 75(5):056401, 2012.
- [12] F. S. Mehmet. *Engineering Optics*. Marmara University, 2015. Fourier Optics.
- [13] B. E. Saleh, M. C. Teich. *Fundamentals of photonics*. John Wiley & Sons, 1991.
- [14] N. George. *Fourier Optics*. Hajim School of Engineering & Applied Science, 2012.
- [15] A. Bettini. *Le onde e la luce*. Decibel, Zanichelli, 1993.
- [16] F.G. Smith, J.H. Thomson. *Optics*. John Wiley & Sons Ltd, 1975.
- [17] V. N. Mahajan. Strehl ratio for primary aberrations: some analytical results for circular and annular pupil. *Journal of the Optical Society of America*, 72: 9:1258–1266, 1982.
- [18] M. Born, Emil Wolf. *Principle of optics*. Cambridge University Press, 1999.
- [19] E.P. Goodwin, J.C. Wyant. *Field Guide to Interferometric Optical Testing*. SPIE, 2006.
- [20] J.W. Krieger. Spim optics theoretical basics. 101, 2013.
- [21] D. Marcuse. *Light Transmission Optics*. Van Nostrand Reinhold Company, 1982.
- [22] J. Schreiber, P. R. Bolton, K. Parodi. Hands-on laser-driven ion acceleration: A primer for laserdriven source development and potential applications. *Review of Scientific Instruments*, 87, 071101, July 2016.
- [23] J. Fuchs, P. Antici, et al. Laser-driven proton scaling laws and new paths towards energy increase. *Nature physics*, 2:10.1038/nphys199, 2006.
- [24] J. Hartmann. From a laser focus to an ion focus. Master's thesis, LMU, 2017.
- [25] M. Speicher. Optical probing for on-target laser contrast measurement. Master's thesis, LMU, 2016.
- [26] K. Nakagawa, A. Iwasaki, et al. Sequentially timed all-optical mapping photography (STAMP). *Nature photonics*, 8:10.1038, 2014.

- [27] UI-5120SE-M-GL Rev.2. uEye. Technical Report (2017-08-01), IDS GmbH, <https://goo.gl/bWHV4H>, 2017.
- [28] D. Joseph. Logarithmic CMOS. In *Image sensors*, 2003.
- [29] PI. *Technical notes H-824 Hexapod Microrobot*, 2013. MS200E.
- [30] J. Alda. Laser and Gaussian Beam Propagation and Transformation. *Encyclopedia of Optical Engineering*, 10.1081/E-EOE, 2003.
- [31] Y.C. Wang, L.H. Shyu, C.P. Chang. The Comparison of Environmental Effects on Michelson and Fabry-Perot Interferometers Utilized for the Displacement Measurement. *Sensors*, 10: 2577-2586, 2010.
- [32] K. Thorn J. Porter, J. E. Lin. *Adaptive Optics for Vision Science Principles, Practices, Design, and Applications*. Wiley-Interscience, 2006.
- [33] S. Herr. Design and Implementation of an Integrated Device for Laser Beam and Target Analysis for Laser Ion Acceleration. Master's thesis, LMU, 2017.
- [34] R.W. Gerchberg, W.O. Saxton. A practical algorithm for the determination of phase from image and diffraction plane pictures. *Optik*, 35: No.2:237–246, 1972.
- [35] J. R. Fienup. Phase retrieval algorithms: a comparison. *Applied optics*, 21:No.15, 1982.
- [36] G. Chaan. Principles of wavefront sensing and reconstruction. *ASP Conference Series*, 2017.
- [37] S. Mezouari and A. R. Harvey. Validity of Fresnel and Fraunhofer approximations in scalar diffraction. *Journal of optics a: pure and applied optics*, 5: 86 - 91, 2003.
- [38] T. M. Jeong, C. M. Kim, D.K. Ko, J. Lee. Reconstruction of Wavefront Aberration of 100-TW Ti:sapphire Laser Pulse Using Phase Retrieval Method. *Journal of the Optical Society of Korea*, 12:No.3:186–191, 2008.
- [39] Z. Liu, C. Guo, J. Tan, Q. Wu, L. Pan, S. Liu. Iterative phase-amplitude retrieval with multiple intensity images at output plane of gyrator transforms. *Journal of Optics (IOP Publishing)*, 17: 025701, 2015.

## Acknowledgments

---

- [40] X. Ouyang, J. Zhu P. Zhu, X. Xie. Output temporal contrast simulation of a large aperture high power short pulse laser system. *High Power Laser Science and Engineering*, 2: No.42, 2014.
- [41] G. R. Brady, J. R. Fienup. Measurement of an optical surface using phase retrieval. *Optical Society of America*, 2006.

# Acknowledgements

In this page I would like to express my deep gratitude to all the people who contributed directly and not to this thesis and my path to it.

I want first of all to thank Prof. Jörg Schreiber for having accepted me in his group. Without him I would not have been aware of the potentialities and relevance of the project I have worked on. His way of finding the physical meaning, even behind the smallest detail, has always amazed me.

A special ‘thanks’ goes to my supervisor, Daniel Haffa, who patiently guided me from the basic knowledge of lasers and optics until the study of complicated systems. He always encouraged me with new suggestions to overcome the problems I faced.

I must thank Martin Speicher for having made the endless afternoons in the office less boring and for having shared his deep knowledge about the optical probing, sport and Paint.net. My thanks go also to Jens Hartmann, who has taught me most of the “just technicalities”, which allowed me to have experimental results from simple ideas. Without him I would have never known what could possibly go wrong during any experiment. I am deeply indebted to Jianhui Bin, who has always answered my stupid questions, for his very helpful sketches. Besides, I want to thank Christian Kreuzer, Johannes Gebhard and all the people mentioned so far for having reviewed and corrected this thesis and my reports.

All the other colleges have not only been interesting people, but have given generously of their time and provided answers and questions that have been invaluable to my studies.

I cannot not mention my friends in Munich and in Italy, in particular, Christoph Becker and Angelo Balestra, who have made my master studies unique and unforgettable.

I want to say a huge “Grazie!” to my family, who supported my studies not only financially but also morally.

Without my girlfriend, Cristina, and her overwhelming love this thesis could not simply exist.

Last but not the least, to God go my biggest thanks. This thesis is dedicated to You.



# **Erklärung**

Hiermit erkläre ich, die vorliegende Arbeit selbständig verfasst zu haben und keine anderen als die in der Arbeit angegebenen Quellen und Hilfsmittel benutzt zu haben.

München, 04.10.2017

---

(Enrico Ridente)